Nano silver-iron-reduced graphene oxide modified titanium dioxide photocatalyst for the remediation of organic dye in water systems

Danielle Sass

(BSc Honours)

A mini-thesis submitted in partial fulfilment of the requirements for the degree of

Magister Scientiae in Nanoscience

Faculty of Science
University of the Western Cape
Bellville, Cape Town, South Africa

Supervisor: Dr Natasha Ross

Co-supervisor: Prof Emmanuel Iwuoha

February 2018

Nano silver-Iron-reduced graphene oxide modified titanium dioxide photocatalyst for the remediation of Organic dye in water systems

Keywords

Photocatalysis

Titanium Dioxide

Nanocomposite

Silver-Iron

Methyl orange/Orange II dye

Photocatalytic study

Band gap

Abstract

Drinking water with high concentrations of inorganic and organic contaminants can cause adverse health defects. Specifically methyl orange dye is an organic water contaminant that has been known (along with others like methyl blue etc.) to have an increase in our water systems over the past few years due to increasing demand in industrial processes. It is therefore of utmost importance to remediate organic contaminants and ultimately enable prevention. The contaminants can be removed by photocatalysis. Anatase TiO_2 is known for its photocatalytic degradation of environmental pollutants and photoelectro–chemical conversion of solar energy. However its application is limited since it is a wide band gap semiconductor, (Eg = 3.2 eV). The following study deals with the enhancement of the photocatalytic properties of TiO_2 for remediation of organic water contaminants. The study was carried out to produce the two nanocomposites AgFe-TiO_2 and AgFe-TiO_2-rGO photocatalyst which purpose is to be cheap and easy to apply, with improved (fast and effective) photocatalytic degradation of methyl orange. The main objective was to decrease the band gap and to introduce intra-band gap states to absorb visible light. Modification of the TiO_2 with small bandgap semiconductor, graphene and Ag- Fe nanoalloy reduced the bandgap energy for visible light absorption and photocatalytic degradation of methyl orange dye. The two composites were synthesised using sonication and chemical synthesis methods. A photocatalytic study (degradation of methyl orange dye) was carried out using a system incorporating an UV lamp source to determine the degradation of methyl orange catalysed by the synthesised photocatalysts AgFe-TiO_2-rGO and AgFe-TiO_2 along with UV-vis Spectroscopy. Morphological studies were carried out using HRSEM and HRTEM which determined the spherical agglomerated nature of AgFe-TiO_2 and the sheet-like nature of AgFe-TiO_2-rGO containing spherical agglomerants but that also contained pockets formed by the sheets of the rGO. XRD served as confirmation of the phase of TiO_2 in both composites to be anatase. Analysis confirmed the formation and elemental

determination of both composites. It was observed that the Band gap of TiO_2 degussa decreased from 2.94 eV to 2.77 eV in the composite AgFe-TiO_2. The photocatalytic reactivity of AgFe-TiO_2 was an improvement from TiO_2 and AgFe-TiO_2-rGO based on the photocatalytic study. Therefore concluding that AgFe-TiO_2 was the best catalyst to convert the dye (Orange II) into free radicals and ultimately remove the contaminant from the water compared to AgFe-TiO_2-rGO.

Declaration

I declare that *"Nano silver-Iron-reduced graphene oxide modified titanium dioxide photocatalyst for the remediation of Organic dye in water systems"* is my work, that is has not been submitted before for any degree or examination in any other university, and that all the sources I have used or quoted have been indicated or acknowledged as complete references.

Danielle Thandi Sass February 2018

Signed ……....................

Dedication

This work is dedicated to : First and foremost God, my parents Daniel Hendrick Sass and Brenda Magdalena Sass, my grandparents Katrina Sass and William Petersen and my late grandparents Joan Petersen and Karel Sass. And everyone who displayed belief and pride in me.

Acknowledgements

"It is of the Lord's mercies that we are not consumed, because His compassions fail not[22]*. They are new every morning: great is thy failtfulness*[23]*. The Lord is my portion, saith my soul; therefore will I hope in Him*[24]*"*- Lamentations 3: 22 – 24. It is with this scripture verse that I thank God almighty For His blessings and faithfulness that are never-ending and that has carried me throughout this practical and theoretical process. I owe this all to Him.

I would like to thank my supervisor, Dr. Natasha Ross for her guidance, encouragement and care throughout the year may you be blessed. To my co-supervisor Prof Emmanuel Iwuoha thank you for the support, advice as well as the chance to be a part of the Sensorlab group at UWC. Thank you to Dr Milua Masikini for your contribution to my practical process.

A special thanks to all my friends and colleagues, Shane willenberg, Nolukholo Tyombo, Kaylin Januarie, Tayla Martin, Meryck Ward, the rest of the Sensorlab group and the Nanoscience group of 2016. Thank you for your continuous support and assistance throughout this process.

I would also like to the Nanoscience programme organisers including Prof Dirk Knoesen, Valencia Jamalie as well as the DST for the funding provided for the completion of this programme. And finally the Department of Chemistry at UWC for providing me the opportunity to study this postgraduate degree.

Finally, I would like to say thank you to my sincerely loved family including my father Daniel Sass, my mother Brenda Sass, my two sisters Charis Sass and Kamara Sass, etc. for their patience, love and support that kept me grounded.

Table of Contents

List of Figures

List of Tables

Chapter 1

Most communities in South Africa are water stressed. To pipe water from fresh, clean sources to arid and rural areas is a costly endeavour. Thus surface water is the only water source [1]. Since this is the main source of water for most we run the risk and we constantly have to be aware of the factors affecting the purity of that source. This also means that we need to apply energy and research into recycling the water used and this can be done at a mass scale by industries where water is used extensively in product manufacturing and many different industrial processes where organic and inorganic contaminants are a product thereof. One of the biggest rising contaminant producing industry would be the textile industry (textile effluent). These include organic contaminants like industrial dyes, phenol derivatives and halocarbons and are of the main contaminants that require safe removal[2]. One of the most harmful dyes in particular is Methyl orange dye/orange II ($C_{14}H_{14}N_3NaO3S$). Even the slightest quantity (1 ppm) is visible and therefore is unfit for human consumption. It has a high health risk as it can cause the sensitization of the skin since it has mutagenic properties, this substance is also highly toxic if ingested according to its statement of hazardous nature[3]. Therefore it is important to ensure a safe way of methyl orange removal.

Methyl orange can be removed by electrochemical treatment, adsorption, chemical precipitation and coagulation –flocculation[4]. A cheaper alternative is through heterogeneous photocatalysis. This method harnesses UV radiation from sunlight or artificial light to speed up the rate at which methyl orange converts into producing free radicals. To date, the most used photocatalyst is TiO_2 due to its photo-stability, low cost, biological and chemical inertness. Since Africa has abundant solar energy; the application of TiO_2 for methyl orange remediation is economically viable. Irradiation of TiO_2 by ultraviolet light creates electron-hole pairs and leads to a chain of redox reactions[4]. Unfortunately, TiO_2 is a wide band gap semiconductor (Eg = 3.2 eV) [6] and possesses certain limitations such as poor absorption of visible light and rapid recombination of the photogenerated electron/hole pairs. However, by increasing the surface area and the population of active sites for catalytic reaction, and by reducing the band gap energy [7], visible light photocatalysis becomes possible[8]. Various investigations have established that TiO_2 is much more effective as a photocatalyst in the form of nanotubes (NTs) and nanospheres (NS), allowing better control of the chemical or physical behaviour [8-10]. Concomitantly, TiO_2 NTs and NSs can be functionalized by incorporation of metal ions [11-15] . In this regard, the low band-gap/no-band gap semiconductor reduced graphene oxide will be used to enhance light absorption ability and charge separation efficiency [6]. The downside of reduced graphene oxide is its variable conductivity when synthesised with another material. To metal-semiconductor combinations have been explored [21]. It is reported that silver, in particular, can facilitate interfacial electron transfer in the composite by acting as an electron-conduction bridge and is conducive to retarding electron–hole recombination [22]. Consequently, the graphene-Ag-TiO_2 catalyst prepared by an impregnation method has proven favourable for photocatalytic degradation of methyl orange and phenol as compared to bare TiO_2 or reduced graphene oxide [23]. While this catalyst has good redox potential, it still requires longer time periods for optimum conversions. The focus of this study is to exploit the synergy of reduced graphene oxide–TiO_2, functionalized with Ag-Fe bimetal, by using a hydrothermal, sonication and hummers method etc. to produce a novel catalyst to enhance the photocatalytic degradation of methyl orange. Both Ag and Fe are considered as suitable substances for photocatalysis due to their low cost compared to platinum-group metals [25-26.] According to crystal field theory[27], their photo-induced reduction promotes redox activity [28]. A low band gap, visible light absorption, fast electron diffusion and fast rate for methyl orange degradation, will be the gold standard to most accurately evaluate the photocatalyst quality. The rGO-AgFe-TiO_2 photocatalyst was expected to meet these requirements due to the applied band gap engineering [29-34]. Here, the reduced graphene oxide will contribute toward expansion of the absorption spectrum into the visible range whilst AgFe enhances the redox activity [35]. In this study the photocatalytic degradation power of rGO–AgFe-TiO_2 with AgFe/TiO_2 and TiO_2 (with and without the presence of hole scavengers) was compared towards fast and effective degradation of methyl orange from contaminated water.

Chapter 2

2.1 South Africa's water situation

The term water is used more and more every day in South Africa. People are constantly being reminded to make sure they use it sparingly and not abuse it, but to reuse it. But with our current water crises the people are finding it difficult to adhere to water restrictions. Besides this issue there are still people needing clean water, we are failing them on a daily basis. The water restrictions have been shifting our entire focus because while people are not adhering to the water restrictions, others don't even have the privilege to access clean drinkable water. Water is scarce and this is becoming more and more evident everyday especially in South Africa. Rainfall levels have decreased to an average of roughly 470 mm per annum in contrast with the world where the average is 857 mm per annum[39]. This is an alarming fact that has the country more aware of the situation than ever before especially with day zero approaching in Cape Town. This has government looking into many alternative solutions for water sources, water reuse and water purification.

A recent environmental legislation in South Africa encourages the sustainable development[39]. The South African government now promotes pollution prevention along with the Department of Environmental Affairs and tourism (DEAT) and Department of Water Affairs and Forestry (DWAF) [39]. It was however discovered that the Metal finishing and Textile sectors are the main contributors to pollution[39].

2.2 Water contaminants

There are so many contributors to the contamination/pollution of water. The two main groups of water pollution are siltation and anthropogenic. Siltation includes mineral particles and soil.

This type of contamination occurs in most water bodies and it is caused by eg. Deforestation which allows for runoff and silt to be carried from mountains into lakes, rivers and streams. Anthropogenic Domestic pollutants (sewage waste); industrialisation, Agriculture wastes that go into lakes, rivers and streams as well as seas and chemical pollution from industries[40].

Domestic pollutants is a vessel for pathogenic (disease causing) microorganisms like protozoa, bacteria, fungi and algae making it infected. Infected water can cause dysentery, thyphoid and gastroenteritis etc[41]. Contaminated water may carry certain bacteria that causes diseases such as hepatitis and possibly cancer which are resistant[41-42]. These bacteria are also responsible for deoxygenation of water bodies which in turn can prove to be dire for aquatic life[41].

Agricultural wastes such as fertilizers, pesticides and manure, waste from farms salts and silt are drained as runoff from agricultural land[39-41]. Bodies of water then tend to become rich in nutrients like nitrates and phosphates which are very harmful to humans and especially to children[41]. Pesticides like DDT, malathion and aldrin are one of the main causes of serious health issues[41-42]. Some of these chemicals are extremely toxic when ingested and metabolised by animals which in turn are then proned to effect humans when we consume these animals[42]. This then leads to hormonal imbalances and may cause cancer[39-41].

Industrialisation tends to contribute to water pollution because many industries are prone to be in close proximity to water bodies since water plays a huge role in most of the industrial processes[41]. The disadvantage of this is that they are responsible for the discharging of untreated effluents into those water bodies[41]. These effluents contain very toxic heavy metals like lead, mercury and arsenic as well as harmful organic and inorganic wastes such as cyanides, acids alkalides, chlorides and dyes etc[40-41]. Majority of these contaminants are not environmentally friendly and are not biodegradable, thus making the water unsafe to drink. The result of consumption of, for example mercury and dyes are poisoning of aquatic life, are birth defects or even death[42].

As previously mentioned the textile and metal finishing sector are two of the main contributors to water contamination/pollution which fall under the industrial group of water pollutants[40]. Of the two the textile industry is slowly becoming a greater factor affecting water pollution. The water effluent from this sector usually have a high chemical oxygen demand and are likely to be coloured[40]. Dyeing, scouring, desizing operations are where most of the organic pollutants emanate from. Majority of these impurities come from the removal of fibres during processing[39-40]. Examples of these Dyes found in the wastewaters of the textile sector is malachite, azine and methyl group dyes like methyl blue and methyl orange.

2.3 Dyes

Dyes are molecules that give colour. They contain auxochromes and chromophores. The colour of the dye is intensified by the auxochromes. The wavelength of the light that is absorbed by the auxochromes and chromophores determines the many different colours given by the dyes. Their chromophore structure allows for them to be classified into the different categories, namely, reactive, azo, acidic, diazo, basic, anthraquinone and disperse dyes. The textile, dyeing, food and printing industries are the main sources of dye wastewater.

Methyl Orange was just used as a representative for the many other dyes as they have the same effect. It was chosen as a model to represent and test the photocatalytic degradation power of the modified photocatalyst in this study as a means of organic contaminant removal from water and possibly inorganic contaminants.

2.3.1 Methyl Orange

Methyl orange is a dye that is used in the textile industry. Its colour is orange and can be diluted to produce lighter colours like yellow as can be seen in figure 1. Its molecular formula is $C_{14}H_{14}N_3NaO_3S$ and its structural formula can be seen in figure 1[3].

Figure 1: Methyl orange and its structural formula with molecular formula inset

2.3.2 Methods for Dye removal

There are a number of techniques used for the removal of dyes from water electrochemical treatment, Adsorption, coagulation-flocculation, chemical precipitation and photocatalytic degradation.

a) Electrochemical removal of dyes set up and mechanism can be seen in figure 2. The set-up is that of a typical electrochemical cell set up that contains an anode (which in this case is made up of Co_3O_4) and a cathode which in this case is either Sn (Tin) or Zn (Zinc) [44]. There is an electrolyte that also contains methylene blue dye in which the reaction takes place. On the left (Anode) oxidation occurs where you find that oxidation occurs and electrons are produced and water. On the right (cathode) reduction occurs where CO_2 is reduced to HCOOH[44]. On the right there is a UV spectrometer to analyse the degradation of the dye. This method however requires a lot of energy and will be costly to enable to mass degradation of dye.

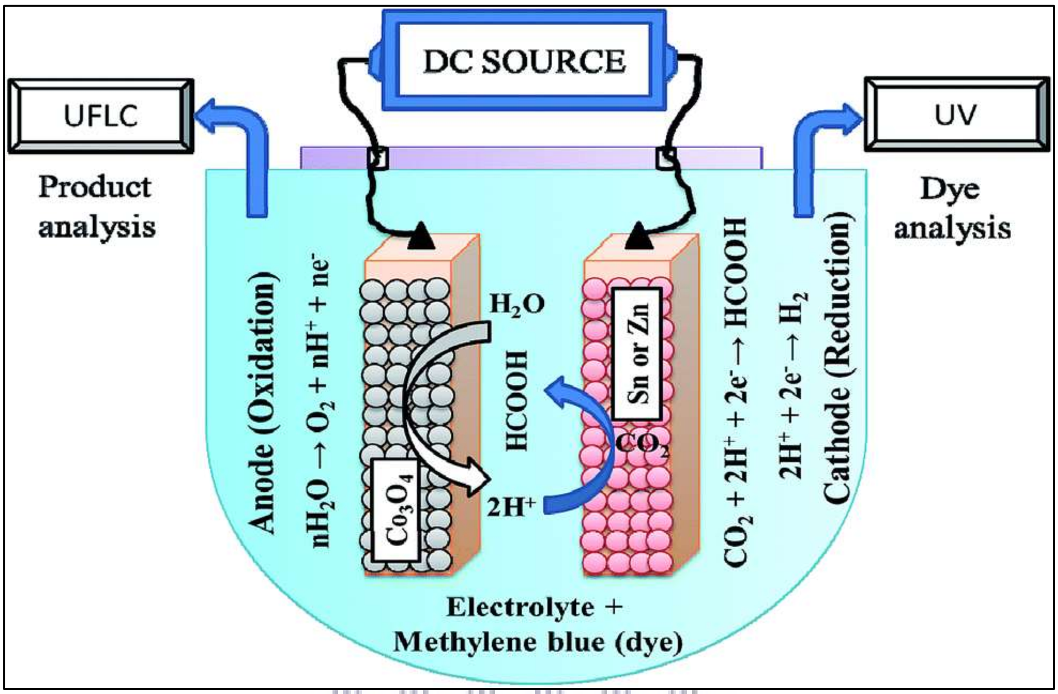

Figure 2: Electrochemical set up of dye removal (Methyl blue) example[44].

b) Adsorption is the most commonly used method. It not only removes dyes but it is also used for the removal of toxic chemicals cyanides and pesticides etc. Essentially this process works on the basic principle of absorption which is the adhesion of ions, atoms, molecules from a liquid (the dye e.g Methyl orange) to a surface[45]. So a film of the dye (adsorbate) is formed on the surface of the activated carbon (absorbant) [45]. The disadvantage of this method however is that the activated carbon is expensive and it has to be reactivated which result in a loss of absorbant of 10-15%[45].

c) Coagulation-flocculation is a process known to make it easier for the removal of the dyes. It is a chemical water treatment that is used before sedimentation and filtration[46]. This then enhances the effiency of sedimentation or filtration. Coagulation is used to neutralise charges and they create a gelatinous mass that traps the particles, this then forms a mass that is large enough to be caught[46]. Flocculation is basically stirring either gently or agitated which then causes the particles to agglomerate into masses big enough to settle and be filtered. The textile waste water is passed through a tank under gentle stirring[46-47]. Thereafter the finely divided suspended solids coalesce into larger particles and settle down. This then is almost similar to chemical precipitation. The complete process can be seen in figure 3. The disadvantages of this system is the toxic chemicals involved, as well as, the fact that it is very time consuming and the system also requires specialised personnel for system maintenance.

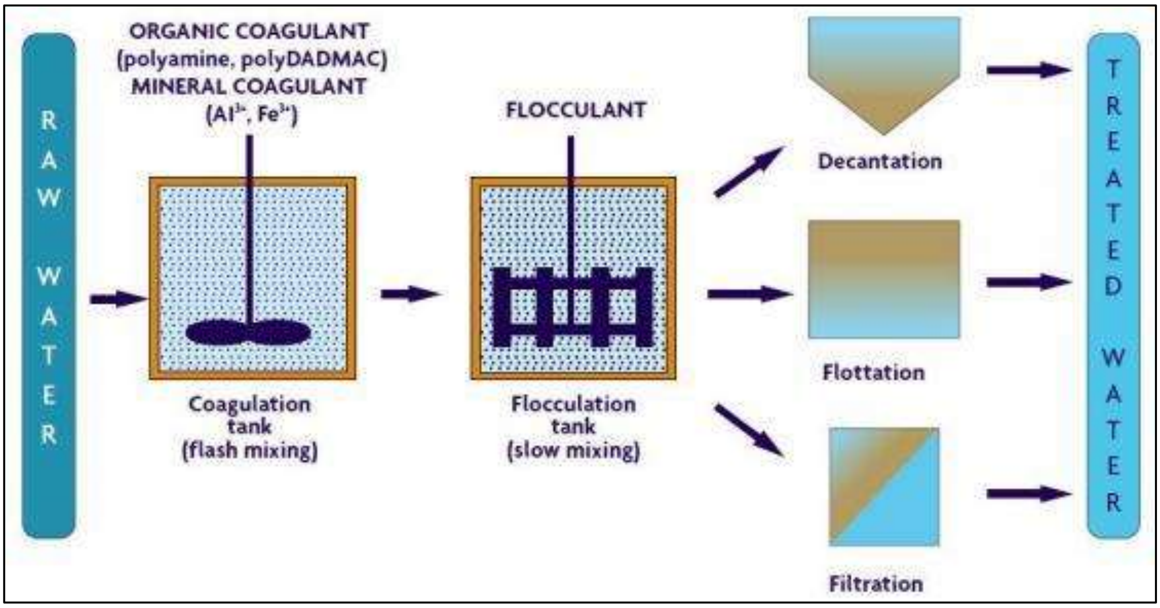

Figure 3: Coagulation-Flocculation set-up[47]

d) Chemical precipitation is basically the formation of solid substance that can be separated from a liquid (solution) [48]. This can happen either by changing the substance into an insoluble form or vice versa where the composition of the solvent is changed to decrease the solubility of the substance in it[48]. The disadvantages are however the high pH’s used in the process, production of large quantities of sludge and it requires a lot of operator control[48].

e) Photocatalysis has been a recent research endeavour that researchers are studying due to the fact that it used UV light, basically sunlight for the reaction to occur at a faster rate implying that there will be less use of energy which lowers the cost. The basic principle makes use of a catalyst that is activated by UV light/sunlight which in turn then speeds up the reaction without taking part in the reaction. Photocatalysis for dye degradation however occurs as seen in figure 4. The process involves the breakdown of dye into free radicals that are less harmful to people and the environment. This all occurs more efficiently when the band gap of the photocatalyst to be used is reduced as can be seen in figure 4 because then more electrons will be able to move to the conduction band since less energy is required for it to travel a smaller distance from the valence band to the conduction band. The advantage depends on the photocatalyst used.

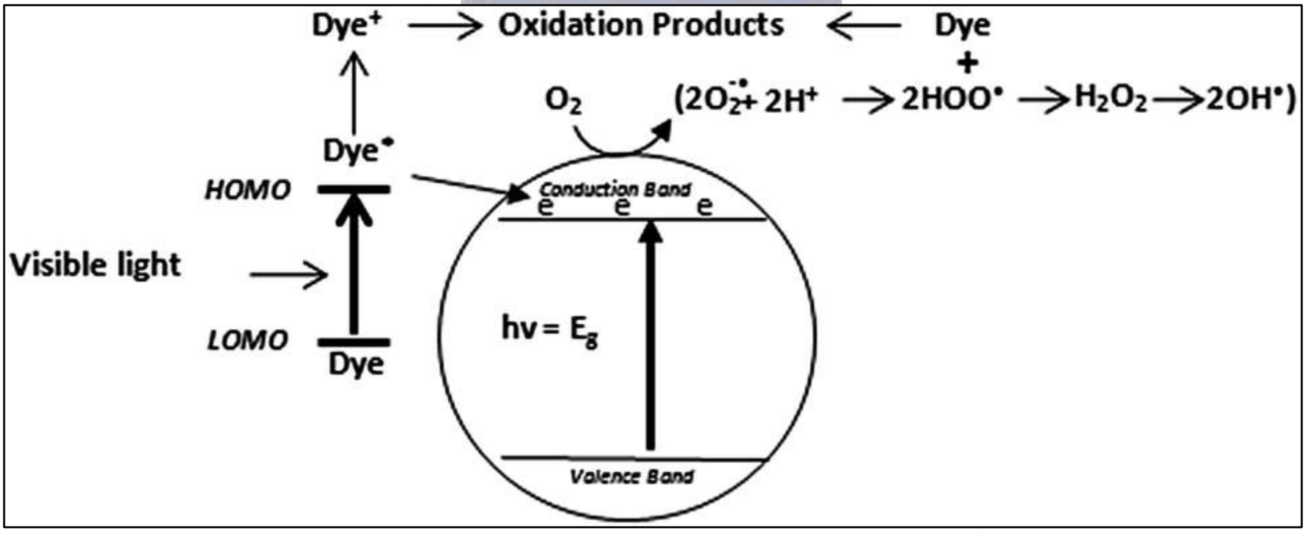

Figure 4: Photocatalyst process for dye degradation[4]

2.4 Photocatalysis

There have been many studies regarding the removal of methyl orange. What has been found is that heterogeneous photocatalyst have been able to degrade aquatic and atmospheric organic contaminants quite efficiently[49]. The sunlight is used in the presence of a photocatalyst to speed up the removal of environmental contaminants while eliminating toxic molecules[49]. The average percentage removal of Methyl orange from wastewater is roughly 50%, it has however been up to 70% with just silver nanoparticles according to Pal, Jolly et al. So this work is said to improve these percentages. Photocatalysis and photocatalytic degradation have various factors that impact its efficiency like temperature, concentration and pH etc. According to Kumar, A and G, Pandey an increase in concentration of photocatalyst increases the efficiency of photocatalysis, also at a pH range of 2 – 4 Methyl orange is removed with greater efficiency.

2.4.1 Photocatalysis of TiO_2

Heterogeneous photocatalysis is basically just when the photocatalyst is in a different phase from the reactants. The field has been rapidly growing in terms of research and use in industry[50]. This is due to its energy, environmental prospects and favourable properties. Photocatalysts such as CdS, TiO_2, WO_3 and ZnO are midst he most common and widely used photocatalyst is TiO_2[50].

Titanium dioxide/Titania. A photocatalyst and compound with potential that extends from energy, purification to medicine and the like[50]. Its extensive use in the photocatalytic field is due to its porosity, surface area, surface hydroxyl group density (this also increases its hydrophilic characteristic), size distribution and crystal structure (anatase and or rutile), and it can be seen in figure 5[50]. Rutile is more stable under high temperatures and has an optical energy band gap of 3.0 eV (415 nm) where as Anatase is the most common form of TiO_2 since it is readily found in nature and it has an optical energy band gap of 3.2 eV (380 nm). Most TiO_2 powders in the rutile phase are spherical and cubic in shape and when it is in anatase phase the particles have a spherical morphology. All of these properties contribute to the electron-hole pairs production, redox process, surface adsorption and desorption process.

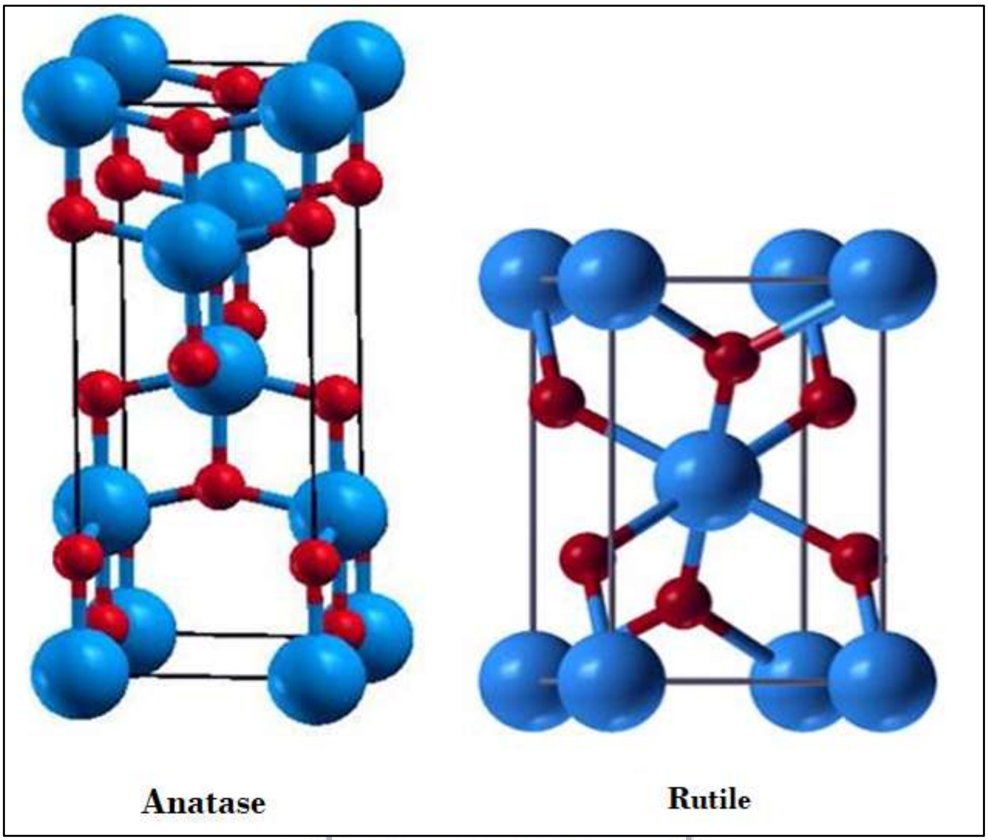

Figure 5: Anatase and Rutile crystal structure of TiO_2[48]

The basic working principle can be defined in a few steps, namely 1) production of electron-hole pairs, 2) photo-generated by excited semiconductor with light energy; 3) separation of electrons and holes by traps available on the TiO_2 surface; 4) a redox process induced by the separated electrons and holes with the adsorbates present on the surface; 5) desorption of the products and reconstruction of the surface, According to Aaron Wold[50] (this can be seen in figure 6). Basically this implies that when the photocatalyst is excited it produces highly oxidising free radicals allowing the destruction of compounds adsorbed on the surface[52].This process can be seen in figure 4. The following shows the mechanism involved in the process explained and illustrated in figure 4. It is known as the hydroxyl radical formation which can be seen in equation 1 - 5.

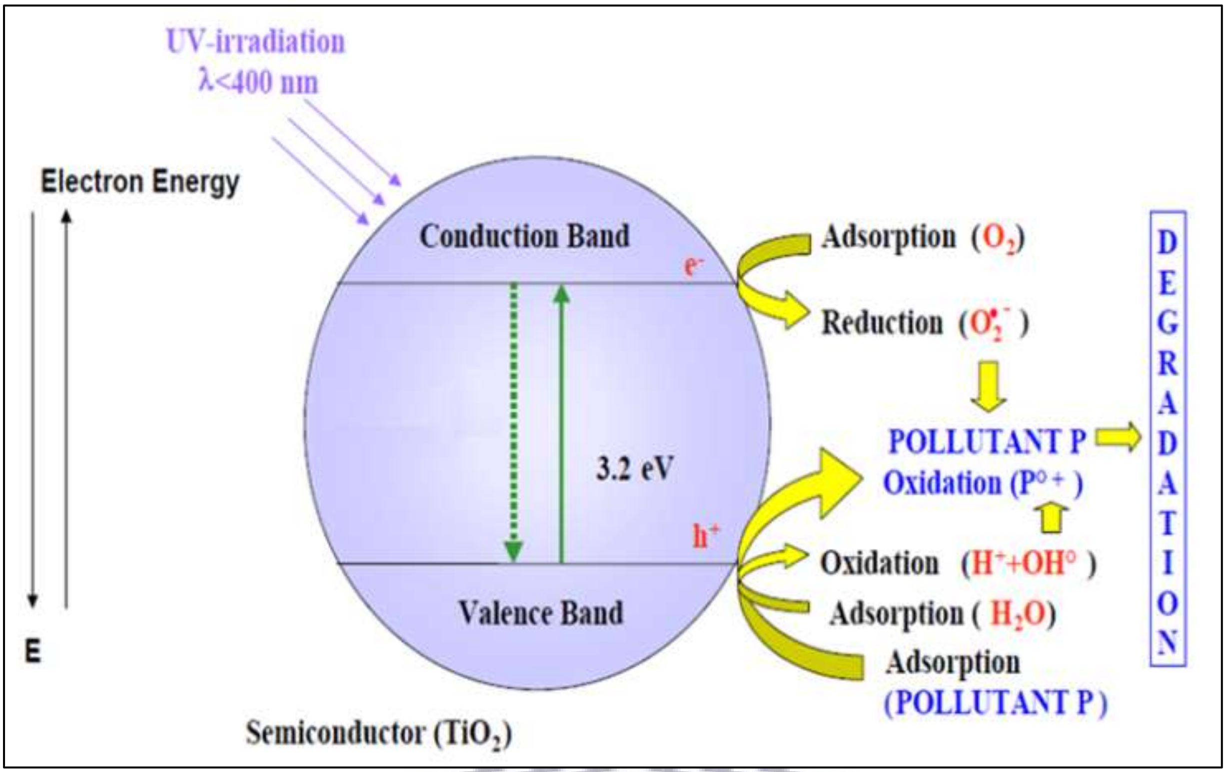

Figure 6: Mechanism for TiO_2 photocatalyst[52]

Research has shown that the photogenerated pair (e^-/h^+: electron/hole pair) react (either reduce and/or oxidize) directly with adsorbed pollutants by either , reactions with water however are leading since water molecules are more abundant compared to other contaminated molecules[52]. The product of water (OH^-) oxidation by the hole produces the hydroxyl radical (•OH) which is a strong oxidant. One of the most important reactions involved in this process is the prevention of recombination of electrons and holes, which results in the accumulation of oxygen radicals that may possibly participate in the degrading of contaminants in solution, which is the reduction of adsorbed oxygen to oxygen radicals. This reaction mechanism is illustrated in equations 1- 5.

1. $TiO_2 + hv = e^-_{cb}(TiO_2) + h^+_{vb}(TiO_2)$
2. $OH^- + h^+_{vb} \rightarrow \cdot OH$
3. $O_2 + e^-_{cb} \rightarrow \cdot O_2^-$
4. $\cdot O_2^- + H^+ \rightarrow \cdot HO_2$
5. $2 \cdot HO_2 \rightarrow O_2 + H_2O_2$
6. $H_2O_2 + \cdot O_2^- \rightarrow OH^- + O_2$

This occurs in all heterogeneous photocatalytic reactions. 1) diffusion of reactants to the surface of TiO_2 , 2) adsorption of reactants onto the surface of semiconductor, 3) reaction on the surface of semiconductor, 4) desorption of products from the surface of the semiconductor and 5) diffusion of products from the surface of the semiconductor [This is according to Elsalamony[52]]. OH radicals can be formed via the reaction of valence band holes either with the adsorbed H_2O or the surface of OH groups on the TiO_2 particle.

Although TiO_2 is a good photocatalyst and been used for its many favourable properties its disadvantage is its band gap that is a barrier for easier movement of electrons from the valence band to the conduction band especially when sunlight is used as a source. Researchers have therefore tapped into experimenting with mixtures of TiO_2, metals and even graphene. This is to reduce its band gap and allow for other improvements.

2.4.2 Titanium Dioxide with Silver Iron and Graphene/reduced graphene oxide

Titanium dioxide's photocatalytic reactivity has been known to improve with the addition of noble metals like Pt, Pd, Ru, and Rh. These were typically used to modify TiO_2 based photocatalysts. These however tend to be costly which is why low cost metals with the same applied performance is used instead[53]. Therefore Iron (Fe) was chosen as an alternative. Besides the fact that Fe is a low cost metal it has been frequently used as a dopant for TiO_2[53]. This is due to its radius of Fe^{3+} (0.64 Å) which is similar to that of Ti^{4+} (0.68 Å), which may allow for an easy incorporation of it into the crystal lattice of TiO_2[53]. Studies have shown that Fe has been able to reduce the band gap TiO_2 to 3.00 eV[55]. Iron is also on its own used as a photocatalyst in the form Fe_2O_3. It is also an environmentally friendly metal and is readily available. Therefore it has been used in this study for the photocatalytic degradation of methyl orange.

Another metal that has researchers experimenting is silver (Ag). Nano-silver is one of the most used nanoparticles in the world. It is being exploited to its favourable properties that include antibacterial which allow for it to act against both gram positive and gram negative bacteria[57]. It has therefore been used in wastewater treatment to act as a disinfectant. It has therefore been known to be environmentally safe[57]. Silver is also known to be a good conductor of electricity. Studies have experimented on the biosynthesised silver (Ag) Nanoparticles for its antibacterial activity and photocatalytic detoxification of dyes such as methylene blue and Congo red and have shown that silver nanoparticles have successfully degraded those dyes[56-57]. Silver has been used as a co-catalyst to TiO_2 for the photocatalytic reduction of nitrates in aqueous solutions and has been proven to be successful in that regard[56]. Therefore it would make it a perfect co-catalyst in to TiO_2 for photocatalytic degradation of dyes like methyl orange.

Both iron and silver has shown to be promising in terms of their properties. It has therefore been looked upon to create a bimetal of the two to enhance their properties and create one metal to act as a co-catalyst to TiO_2. Studies have shown that the nanocomposite Ag-Fe_2O_3 have improved the properties of Fe_2O_3, which as previously mentioned has been used as a photocatalyst[58].

Graphene/reduced graphene oxide has been taking the world by storm due to its vast range of application. It is known for its structure which sheet-like and one atom thick, this can be seen in figure 7. It has unique electronic properties, it is a good heat conductor, it has a large specific surface area and high transparency and this contributes to the facile charge separation and adorptivity in its hybrid structure[59].

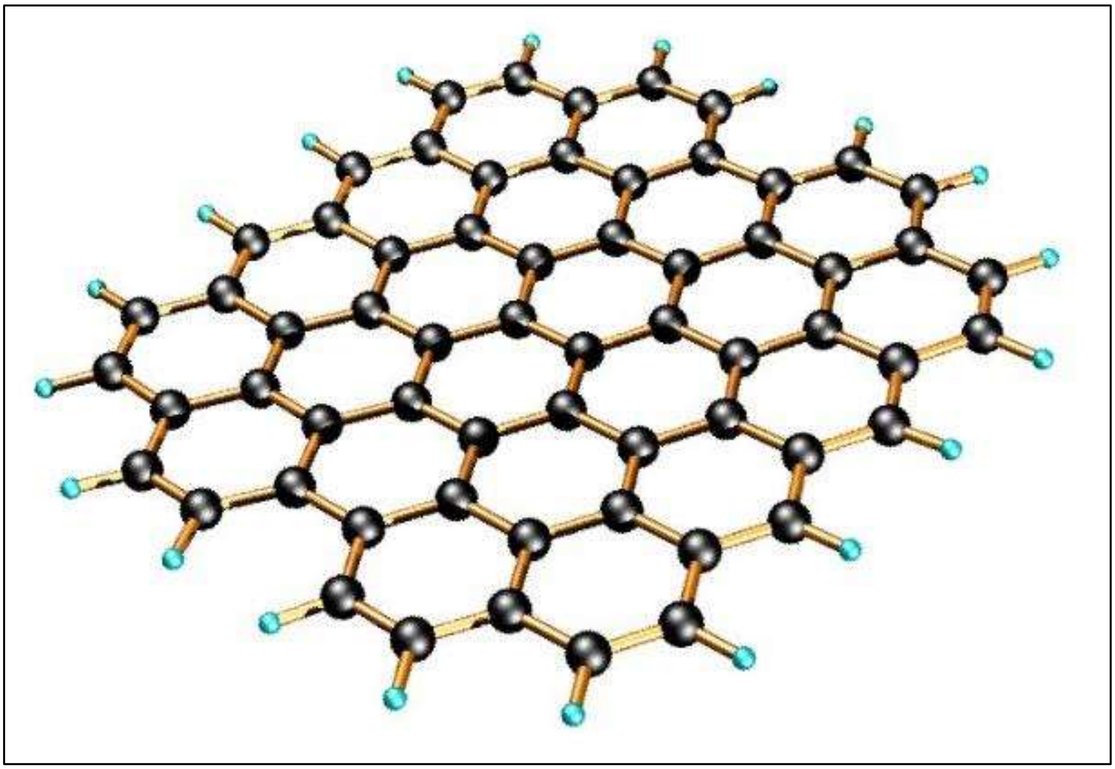

Figure 7: structural formula of graphene[65]

Because of these properties it has been used in the field of photocatalysis. Studies have shown that it has improved catalytic photodegradation under solar light where it has been synthesised in a nanocomposite with TiO_2 nanowires[59]. This similar type of composite synthesised via a sol-gel method has been studied for the use of methyl orange degradation and has shown to improve the photcatalytic activity of TiO_2[60]. This has lead to the incorporation of graphene/reduced graphene oxide into the study for the degradation of methyl orange in water.

This study has therefore been conducted using Silver, Iron as a bimetal and reduced graphene oxide to improve the photocatalytic degradation of methyl orange and therefore dyes in contaminated water. Thus providing a platform for efficient photocatalytic degradation of other organic water contaminants as well as inorganic contaminants such as nitrates which are a serious issue in many parts of the world.

Chapter 3

OVERVIEW

In this chapter, chemical materials, physical equipment and experimental procedures including methods that were used during optimization of the Photocatalytic system are explained. This also includes the outline of the experimental procedure on novel AgFe-rGO nanocomposite to form [TiO_2-AgFe-rGO]. The physical equipment, chemical material and characterization are also in this section.

3.1 Reagents and Materials

The chemicals used in this study are as follows: Sulphuric Acid (99%), Graphite powder, Potassium permanganate (KMnO4), Hydrogen peroxide, Sodium borohydride, silver nitrate, Titanium dioxide nanopowder (99%), Iron-sulphate heptahydrate, Polyvinylpyrrolidone (PVP), sodium hydroxide (NaOH), sulphuric acid (H_2SO_4), graphite powder, Methyl Orange and Hydrogen peroxide (H_2O_2). These were purchased at Sigma-Aldrich.

3.2 Experimental flow diagram of the current study

The following is an experimental flow diagram based on the different aspects ventured in this study. In the schematic flow diagram shown in figure 8, chapter three was divided into four sections. The first section is the optimization of the photocatalytic system where optimized system is established to carry out photocatalytic activity testing using methyl orange dye as the indicator/pollutant. The second section uses the established optimized conditions to carry out photocatalytic analysis. Section three presents the methods used for the materials synthesised in this study. Section four is a list of the characterization techniques involved in the materials analysis.

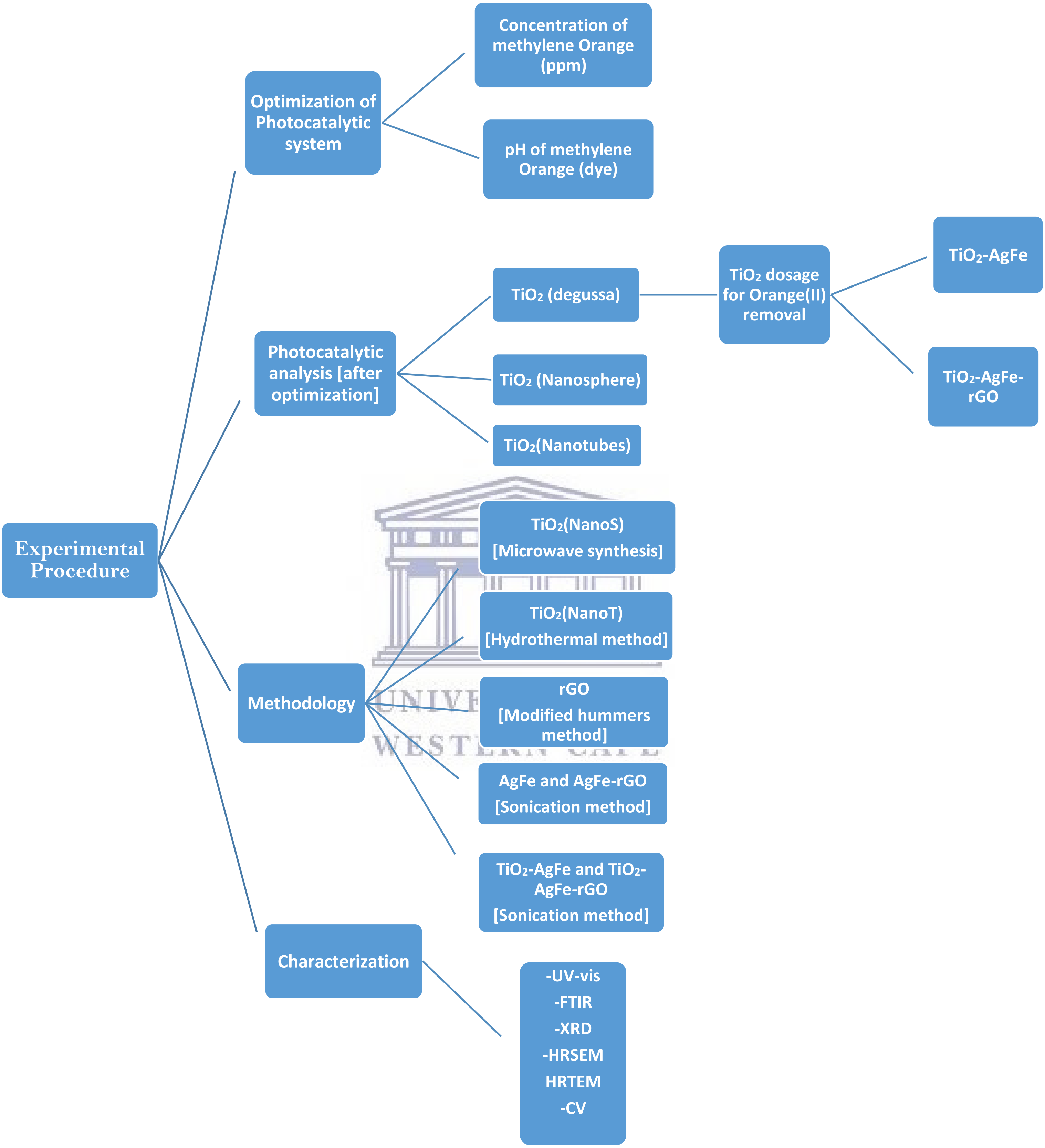

Figure 8: Experimental flow diagram of study

3.3 Methodology

3.3.1 Reduced Graphene Oxide/ Graphene Oxide (modified hummers method)

125 mL conc H_2SO_4 and graphite powder (5 mg) were taken in 500 mL three necked round bottom flask. Potassium permanganate (17.5 g) was gradually added into this flask kept in an ice bath. The mixture was stirred at 35 ^oC and then diluted by adding sufficient amount distilled water in ice bath at 0 ^oC. 30 % hydrogen peroxide was then added until the bubbling of the gas was complete. The product was collected by centrifugation and washed repeatedly with deionized water to remove the residual salts and acids. After purification, the GO suspension was dried under vacuum at 70 ^oC for two days. 100 mg of graphene oxide was dispersed in 100 mL of H_2O and sonicated for 1 hr and 200 mg of $NaBH_4$ was added. The mixture was then stirred for 30 min and heated under reflux at 142 °C for 3 h. The black solid product (rGO) was isolated by centrifugation, washed with water and finally dried.

3.3.2 Titania (TiO_2) nanotubes (hydrothermal synthesis)

TiO_2 powder was placed in a 50 mL Teflon lined autoclave in aqueous NaOH. The solution was then stirred at 300 rpm with the heating rate of 2 ^oC/min from room temperature. When the temperature reached 130 ^oC the time was started for a 3 h reaction. The product was then washed with deionized water until the pH was near 7. This product was then immersed in 300 mL of 0.1 M HCl solution for 1 h. It was then washed again and filtered until the pH reached 7. The product obtained was then dried in an oven at 80 ^oC for 5 h.

3.3.3 Titania (TiO_2) nanospheres (microwave synthesis)

The TiO_2 powder was calcined in an oven at 700 ^oC. 0.15 g of TiO_2 powder was mixed with 50 mL of NaOH (10 M) aqueous solution. This mixture was then sonicated for 5 min and thereafter placed in Teflon tubes for the microwave synthesis process at which the power was 195 W for 90 min. The obtained product was then washed thoroughly with distilled water until pH was roughly 7. It was then filtered and dried under a vacuum at 90 ^oC.

3.3.4 Silver-Iron bimetal nanoparticles

NaOH (200 mL) was mixed with 100 mL methanol solution containing 0.010 mol $FeSO_4.7H_2O$ and 0.001 mol $AgNO_3$ at room temperature under nitrogen atmosphere and constantly stirred for 30 min. The material/product (Ag-Fe) nanoparticles was then collected through vacuum filtration, rinsed thrice with methanol and was then dried under vacuum at 50 ^oC for 10 h.

3.3.5 Ag-Fe/r-GO nanocomposite synthesis

1 g of Graphene Oxide was dipped into a 25 mL coating solution(10 mL absolute ethanol and 15 mL distilled water) containing 0.01 g Polyethylene glycol (PEG) (20 000) and 1.05 g $FeSO_4.7H_2O$. The mixture was mixed intensively (stirring at 1000 r/min) for 30 min and then sonicated for 1.5 h. Then 25 mL of 0.6 mol/L $NaBH_4$ solution (Incl. 12.5 mL absolute ethanol and 12.5 distilled water) was added dropwise to the flask at 0 ^oC for 2 h under sever stirring. This was then washed with distilled water and absolute ethanol three times respectively. 15 mL 2.6 mmol/L $AgNO_3$ was added dropwise to the solution for 2.5 h under sever stirring. The product was then filtrated and dried in an oven at 60 ^oC overnight.

3.3.6 TiO_2-AgFe (sonication method)

Synthesised AgFe bimetal nanoparticle product (0.2 g) was mixed with 1 g TiO_2 (Degussa) nanopowder and 3 mL NaOH(5 M). This was sonicated for 2 h. The material was then centrifuged and washed with water several times. This was then dried at 50 ^{o}C under vaccum for 8 h.

3.3.7 TiO_2-AgFe-rGO (sonication method)

Synthesised AgFe-rGO nanocomposite product (0.2 g) was mixed with 1 g TiO_2 (Degussa) nanopowder and 3 mL NaOH(5M). This was sonicated for 2 h. The material was then centrifuged and washed with water several times. This was then dried at 50 ^{o}C under vaccum for 8 h.

3.4 Characterization of structural properties

Presented below are the techniques and instrumentation compulsory for the characterisation and the analysis/interpretation of the synthesised material.

3.4.1 Surface morphology

3.4.1.1 HRSEM (High resolution Scanning Electron Microscopy)

Scanning electron Microscopy is based on scanning principle based on the interaction between the surface of a material and a focused electron beam to produce a 3D image of the material at an atomic scale. This is possible due to its setup as can be seen in figure 9. An electron source is required to generate an electron beam which can be seen in figure 9 to be the electron gun. The electron beam then travels through a series of apparatus where it is initially accelerated and then focused onto the sample's surface. Secondary electrons reflected off the sample's surface are caught by a detector which is then converted into a 3D image. An example of this is seen in figure 9, this is important for the analysis of the TiO_2-rGO-AgFe photocatalyst shape. Besides secondary electrons X-rays are also reflected off the samples surface which can then be collected and interpreted/converted for element confirmation/composition (EDAX). All of this is done with high resolution for improved atomic scaled materials imagery. The ZEISS ULTRA scanning electron microscope was used for HRSEM analysis.

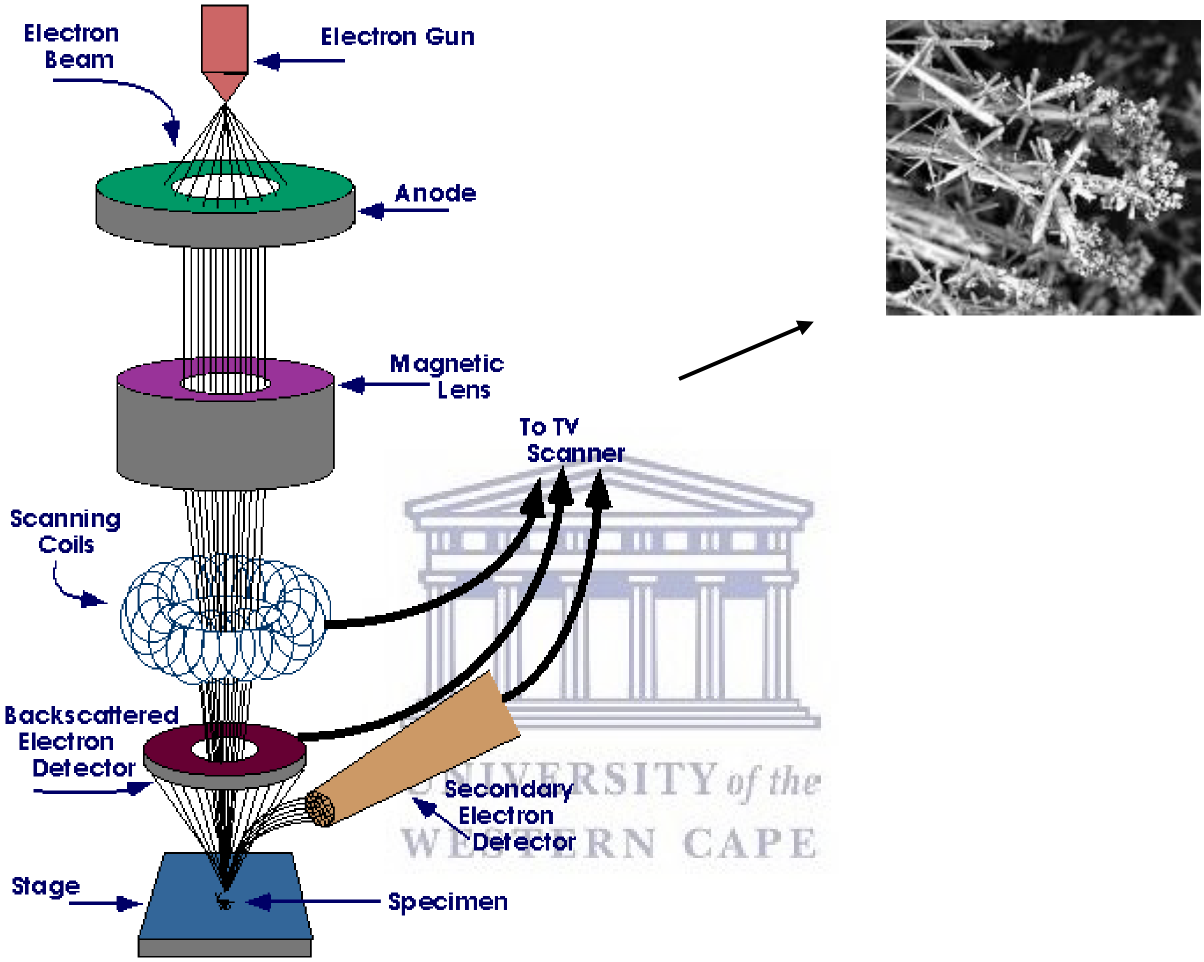

Figure 9: SEM setup and image production example nanocrystals/snowflakes[61]

3.4.1.2 HRTEM (High resolution Transmission Electron Microscopy)

HRTEM has an operating scheme similar to that of HRSEM. The important difference between it and HRSEM is that after the focused beam of electrons interacts with the sample, part of it gets transmitted through the sample. This is then re-focused using objective lenses which is then converted into an image which then can be seen having lighter and darker shades which correlates to the surface being thin and thick (this can be seen in figure 10). Elemental composition of the sample can also be attained through EDS (which is the interpretation of the X-rays into a graph of the elements. Lattice fringes observed on a TEM image allows for the determination of sample crystallinity aswell as D spacing.

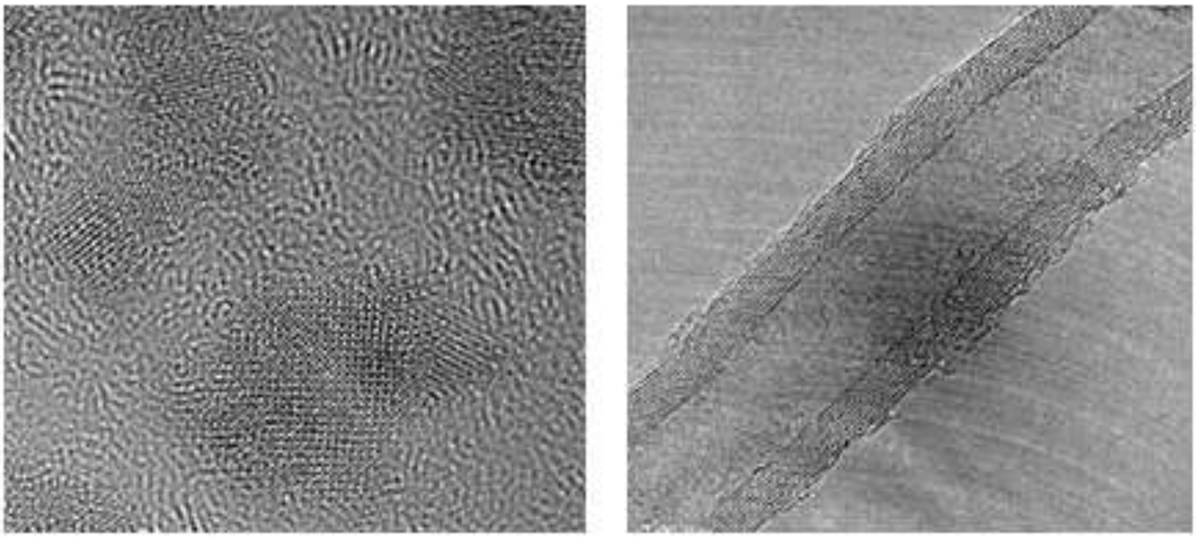

Figure 10: Examples of TEM images[62]

3.4.2 XRD (X-ray Diffraction)

XRD is a technique used to determine the crystal structure of a material. It operates using Braggs law which describes the condition on θ for the constructive interference to be at its strongest where n is a positive integer and λ is the wavelength of the incident wave (this is seen in figure 11). Two different light beams are scattered at the same angle on a crystalline structure. The extra distance travelled by the second beam then enables the determination of the interatomic distance between the planes of atoms. XRD is used in the analysis of materials to identify its crystalline phase and orientation. It’s used to determine structural properties like strain, grain size, transformation, Detection limits, and thickness of films and multi-layers.

Therefore this technique was used to determine the crystalline phase of the materials TiO_2-AgFe-rGO, TiO_2-AgFe, TiO_2 nanopowder and AgFe.

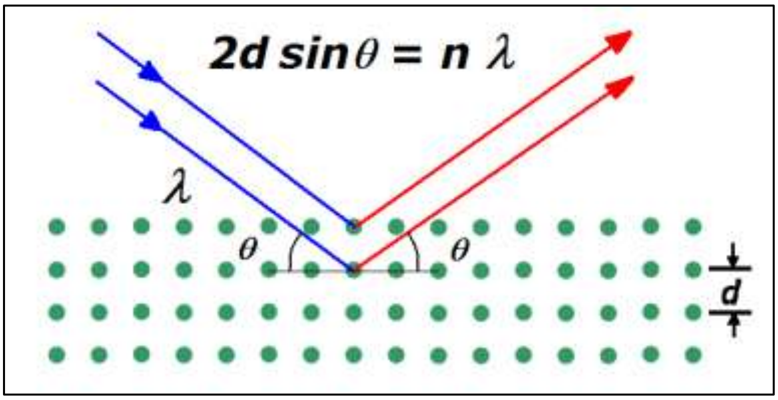

Figure 11: Braggs law diagram[64]

3.4.3 FTIR (Fourier Transform Infrared Spectroscopy)

FTIR is a technique that is based on vibrational spectroscopy that makes use of asymmetric molecular vibration, stretching and rotation of chemical bonds during their exposure to appointed wavelengths of infrared light. When the signal changes from the time domain into its representation in the frequency domain, this is known as Fourier transform. This is detected and can be illustrated in an infrared spectrum. FTIR is used for graphical identification of compounds/element, their functional groups, how many atoms are bonded together, how their pi arrangement is assembled e.g single and double . This technique was used to determine the functional groups in the materials TiO2-AgFe-rGO, TiO2-AgFe, TiO2 nanopowder and AgFe.

3.4.4 UV-vis (Ultraviolet-visible spectroscopy)

UV-vis spectroscopy's working principle is based on Beer Lamberts law ($A = \varepsilon bc$) where A is the measured absorbance, ε is the wavelength-dependent molar absorptivity coefficient, b is the path length and C is the analyte concentration. According to the principle the greater the amount of molecules present in a sample able to absorb light means that the light can expatiate and flow to increase illumination. Therefore it measures the attenuation of a beam of light as it travels through a sample or after it has been reflected off the surface of the sample. The absorbance can then be measured over an enlarged spectral range. The absorbance vs wavelength graph generated from this technique allows for the calculation of the spectral band gap. This can be accomplished when values are extracted from the graph to through further calculations ultimately calculate the band gap, using the followng final formula:

$$E(energy) = \frac{h(Planks\ constant)x\ C(speed\ of\ light)}{\lambda(wavelength)}$$

This technique was used to confirm certain elemental peaks aswell as red or blue shifts. It was also used to calculate the band gap for TiO_2-AgFe-rGO, TiO_2-AgFe, TiO_2 nanopowder

3.4.5 Electrochemical analysis

3.4.5.1 CV (Cyclic voltammetry)

CV is an electrochemical technique that is used to determine the current created by an electrochemical cell via varying the voltage. The set up for this technique can be seen in figure 12 where there are three electrodes namely the Working electrode (glassy carbon electrode), the Reference electrode (Ag/AgCl), and the Counter electrode (platinum wire). The setup was a CH Instrument electrochemical workstation as well as a 600 E potentiostat (USA). The electrolyte solution was made up of LiOH and sample. The experiment was carried out in an argon atmosphere at room temperature. CV was used to determine the anodic and cathodic peaks of the materials TiO_2-AgFe-rGO, TiO_2-AgFe, TiO_2 nanopowder.

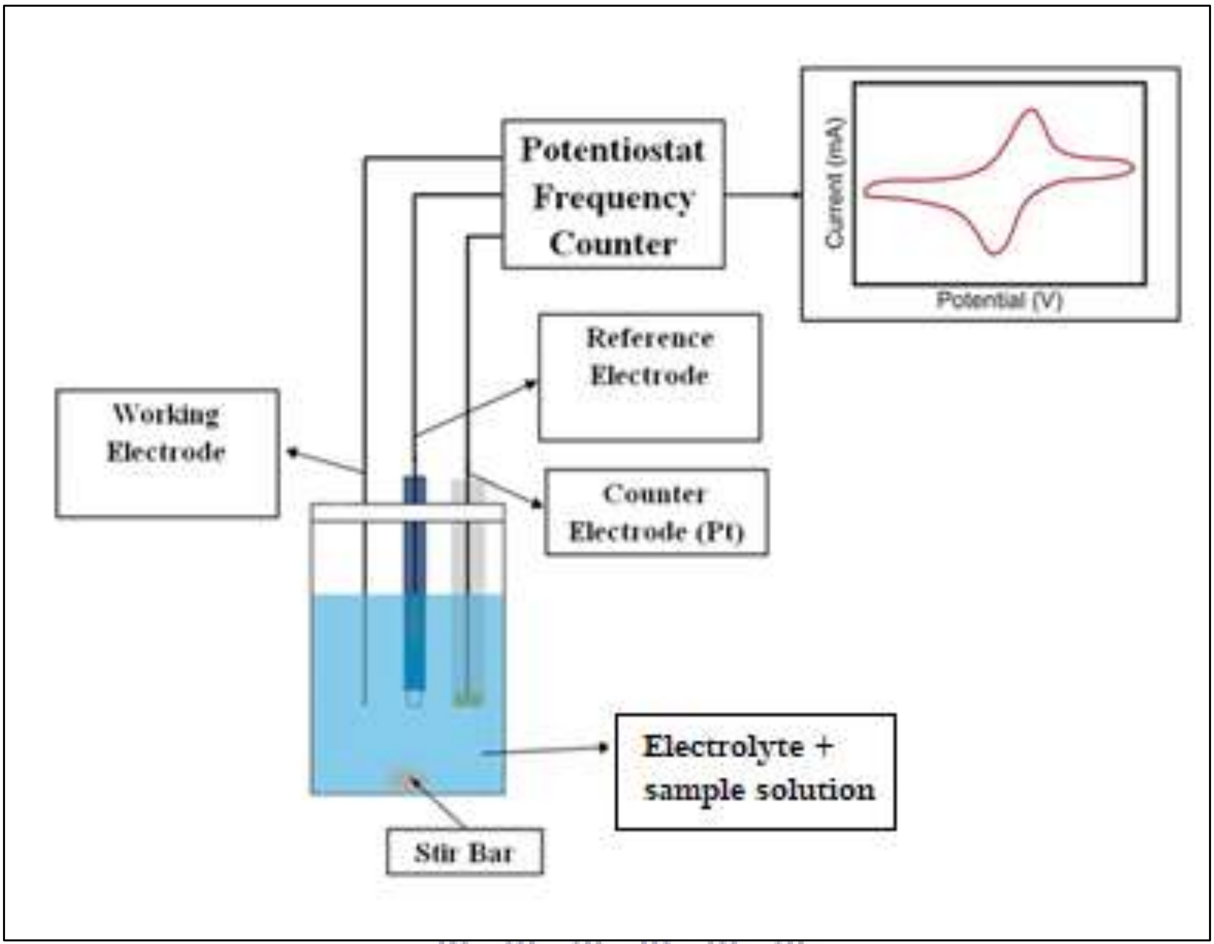

Figure 12: Cyclic voltammetry setup[63]

3.5 Photocatalytic analysis

This subsection describes the photocatalytic reactivity procedure. This process was performed using a few steps described in the following paragraphs. At the end of each timed photocatalytic experiment UV-vis spectroscopy was utilised as an immediate measure of absorbance of the treated and untreated Methyl orange dye. Thereafter the percentage degradation was obtained. The experimental setup will be shown in section 1 and the experimental procedure for system optimization will be seen in section 2.

3.5.1 Experimental setup

As mentioned above methyl orange was used as the pollutant and its percentage degradation was determined through calculations after the different photocatalyst were added. The setup can be seen in figure 13. It consists of a UV lamp, a thick 5mm glass tank which was lined on the inside with aluminium foil, a glass bowl containing the Dye (methyl orange) solution which rested on ice blocks to make sure the system didn't over heat and a magnetic stirrer.

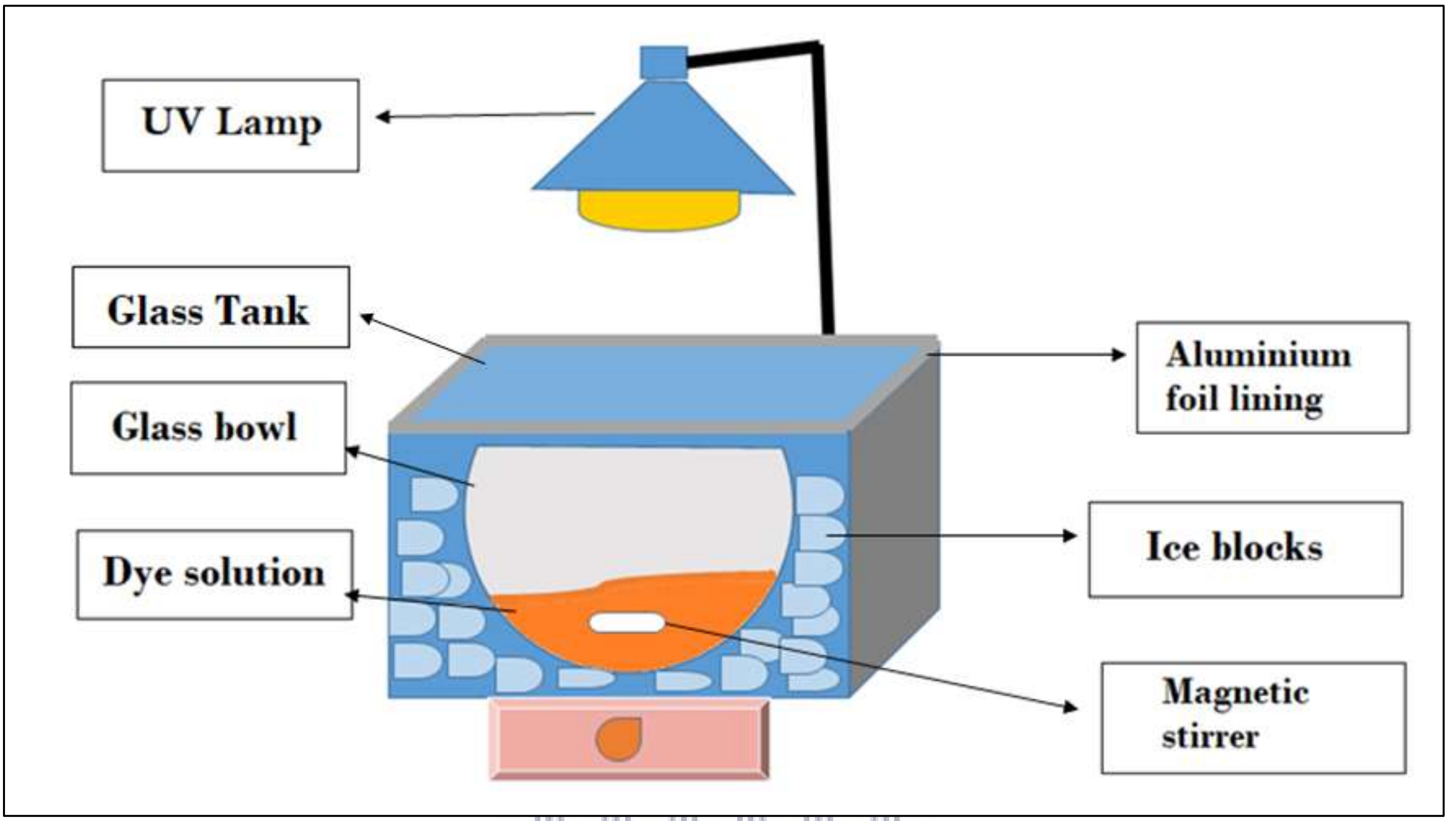

Figure 13: Photocatalytic system

3.5.2 System optimization

There are a few factors that may affect the removal of pollutant in water and hence in the photocatalytic system namely concentration and pH of the pollutant solution. Therefore for optimization those two aspects were investigated to discover its effect on the degradation of orange II dye. Therefore three concentrations and thereafter five pH's of the dye solution was investigated. The degradation percentage was acquired by sampling every 30 minutes in the space of 2 hours. These results were then used to calculate percentage degradation using the formula:

$$Degradation\ \% = [(Co - Ct)/Co]\ \text{x}\ 100$$

The optimum conditions were therefore established to be 4 ppm and pH 2.

Chapter 4 (Results and discussion - Precursors)

This chapter contains the results obtained for the TiO_2 degussa, Fe and AgFe nanobimetal. The results discussed were spectroscopic characterisation technique for bond, elemental and surface analysis. Electrochemical technique was also discussed for redox analysis.

4.1 HRSEM (High resolution Scanning Electron Microscopy)

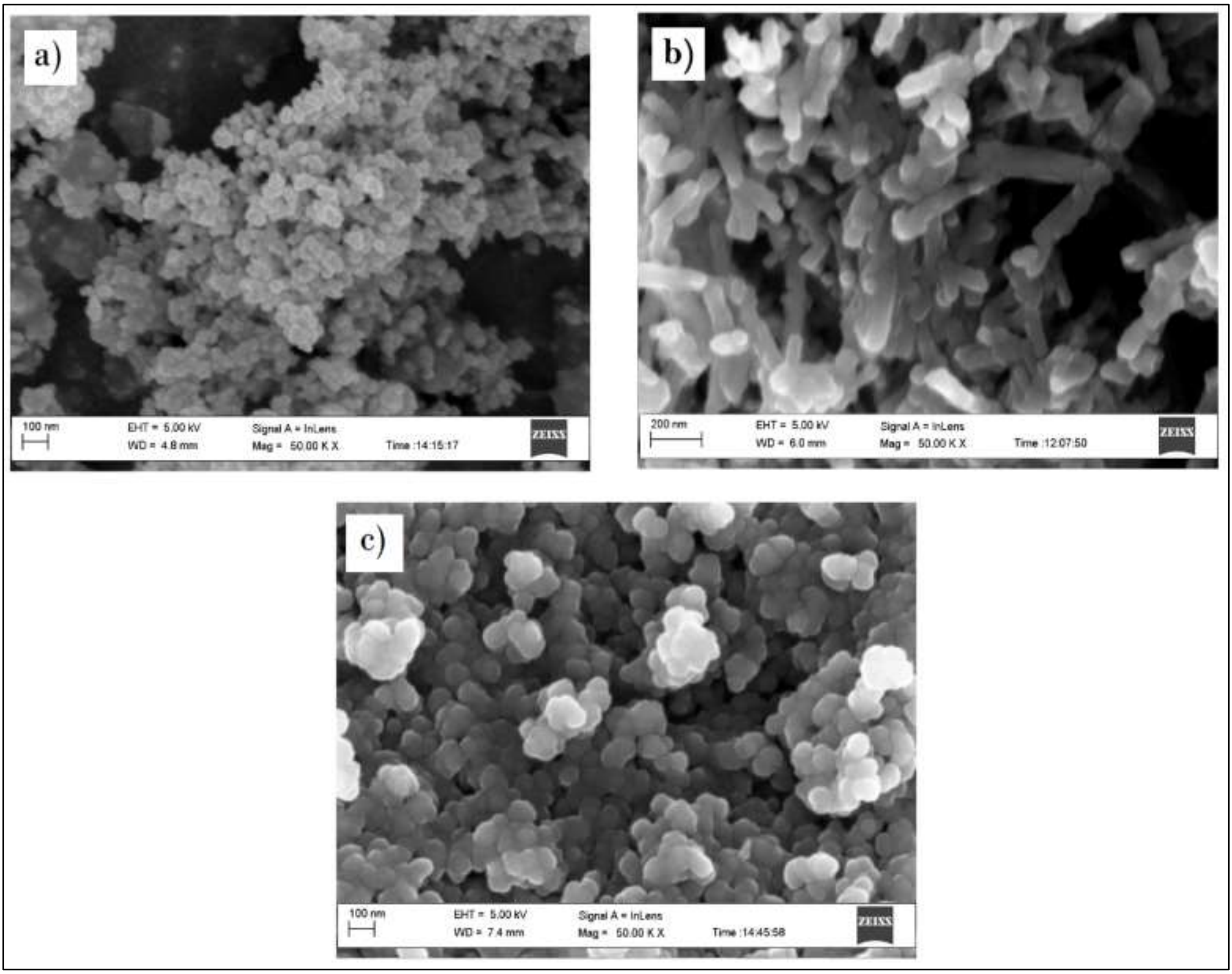

Figure 14: SEM Image illustrating the a) TiO_2 degussa, b) TiO_2 nanotubes and c) TiO_2 nanospheres taken at a magnitude of 50.00 K X

Figure 14 illustrates three different forms of TiO_2. Image a) is the TiO_2 degussa nanopowder which was purchased, in the image you can see that the particles are agglomerated and roughly spherical in shape. They are extremely small (approximately 15-25nm in diameter). This is an indication of good dispersion as it has a large surface area. Image b) is the synthesised TiO_2 nanotubes, it shows long tube-like structures that are on average roughly on 1µm in length and 60nm in width. This indicates that it possibly has a large surface area but since the particles of TiO_2 degussa are smaller it has a greater surface area according to the nanoscience research carried out by Schwarz, James A., Cristian I. Contescu, and Karol Putyera . Image c) is the synthesised TiO_2 nanospheres. The TiO_2 nanospheres were formed however they are agglomerated which in turn creates much larger particles then if they had great separation between each particle. This could be due to the lack of heat/pressure applied during the synthesis of the particles. On average the size should be about 30- 40 nm, however since it has agglomerated the average size has increase to roughly 70- 90 nm in diameter. It was observed that the form of TiO_2 with the greatest surface area is TiO_2 degussa nanopower and this makes sense since b) and c) were both synthesised with TiO_2 degussa as a precursor. Photocatalysis testing was carried out after these to establish the best photocatalyst before further testing was carried out. The result of which concluded that TiO_2 (Degussa) was the best for the remediation of methyl orange from the water, TiO_2 (Degussa) was used further as the best form of TiO_2 for the composites AgFe-TiO and AgFe-TiO_2-rGO.

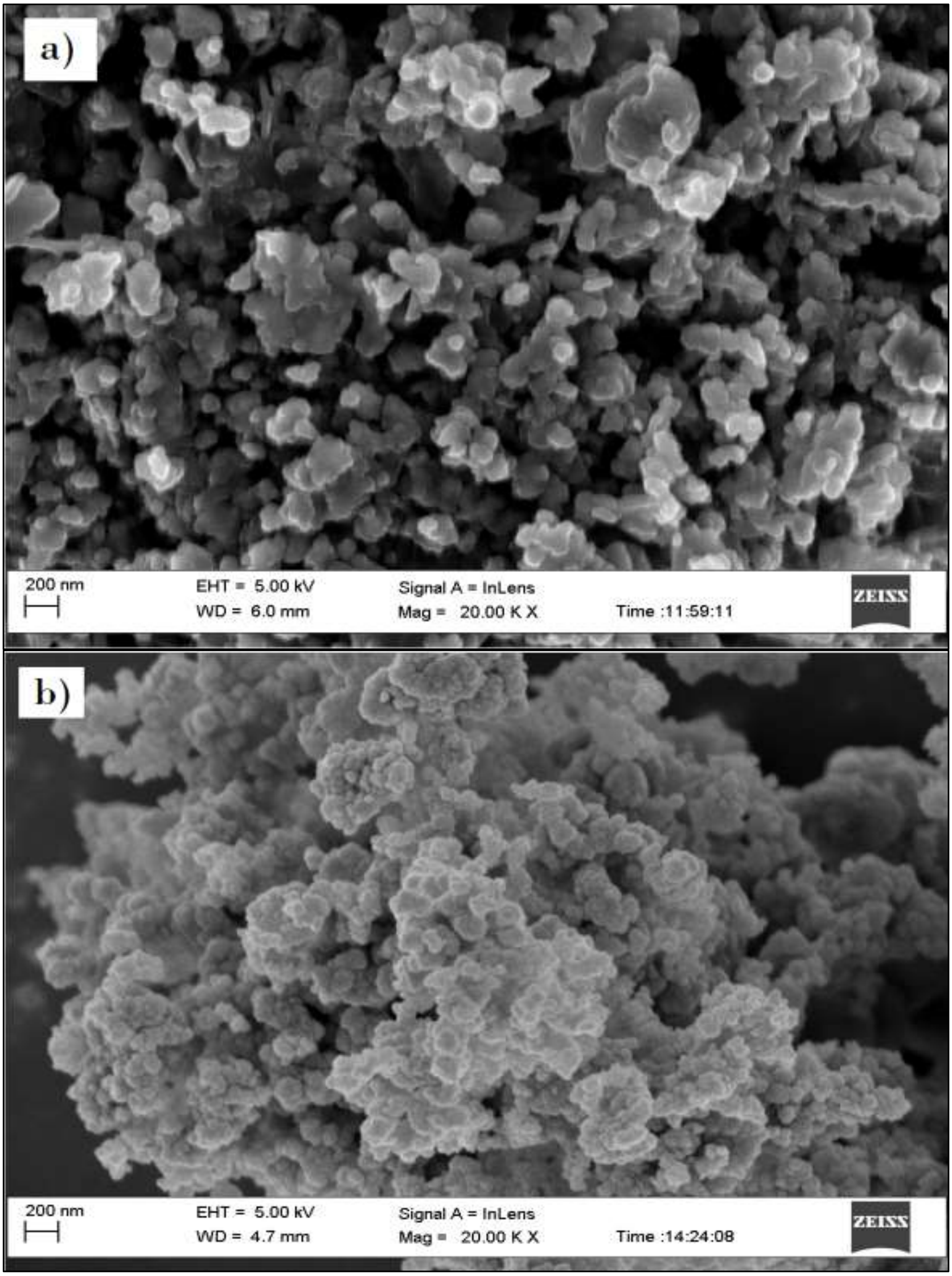

Figure 15: SEM image of a) Fe nanoparticles and b) AgFe nanalloy at a magnitude of 20.00 K X.

Figure 15 a) shows iron nanoparticles that can be seen is not uniform in shape as there are both spherical and rectangular/square-like shapes. All of those shapes are made up of agglomerated individual particles. Also there are more dark shades then light which could be an indication of density[68] and this density has been proven to affect the light absorption properties of photocatalyst[69]. b) shows the formation of fairly spherical-like shapes that are highly agglomerated forming large particles. These agglomerations are also made up of individual Fe nanoparticles covered with Ag nanoparticles which then also allows for the general colour of the particles to be lighter compared to that of just the plain Fe nanoparticles.

4.2 HRTEM (High resolution Transmission Electron Microscopy)

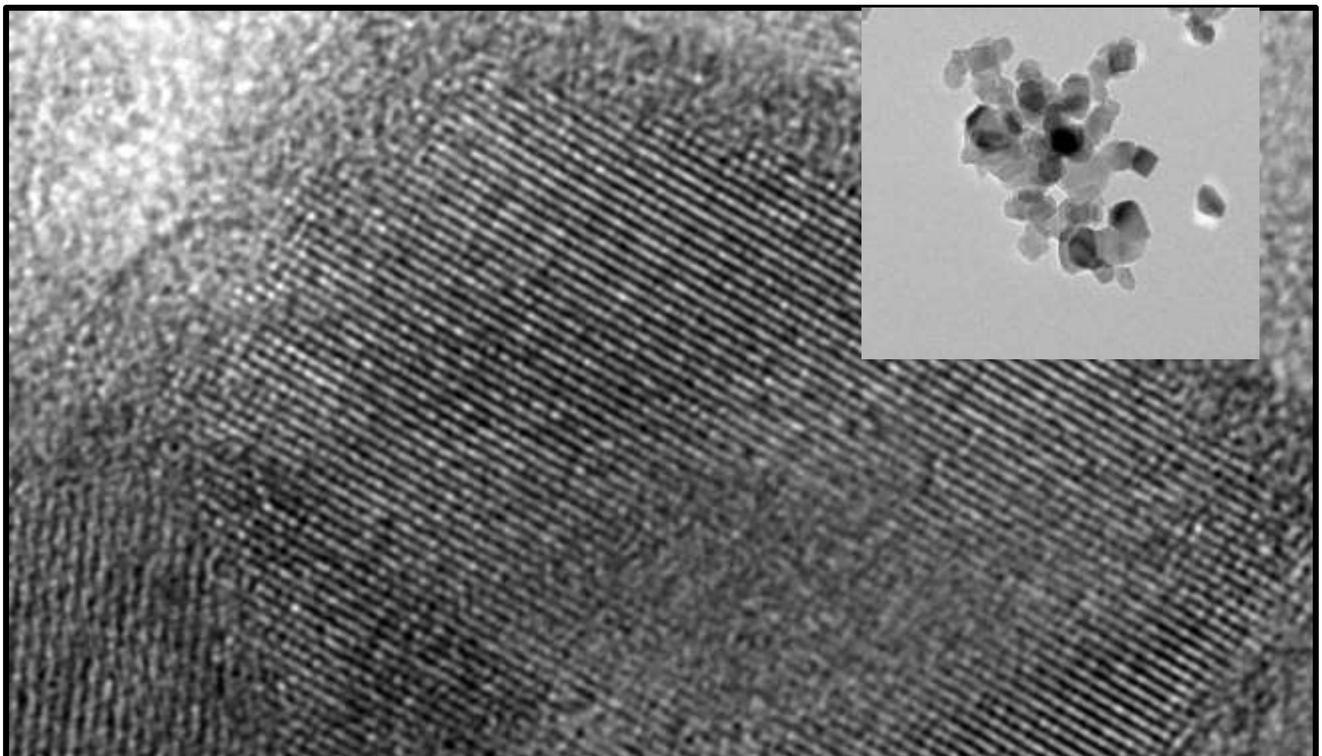

Figure 16: TEM image of TiO_2 degussa with insert.

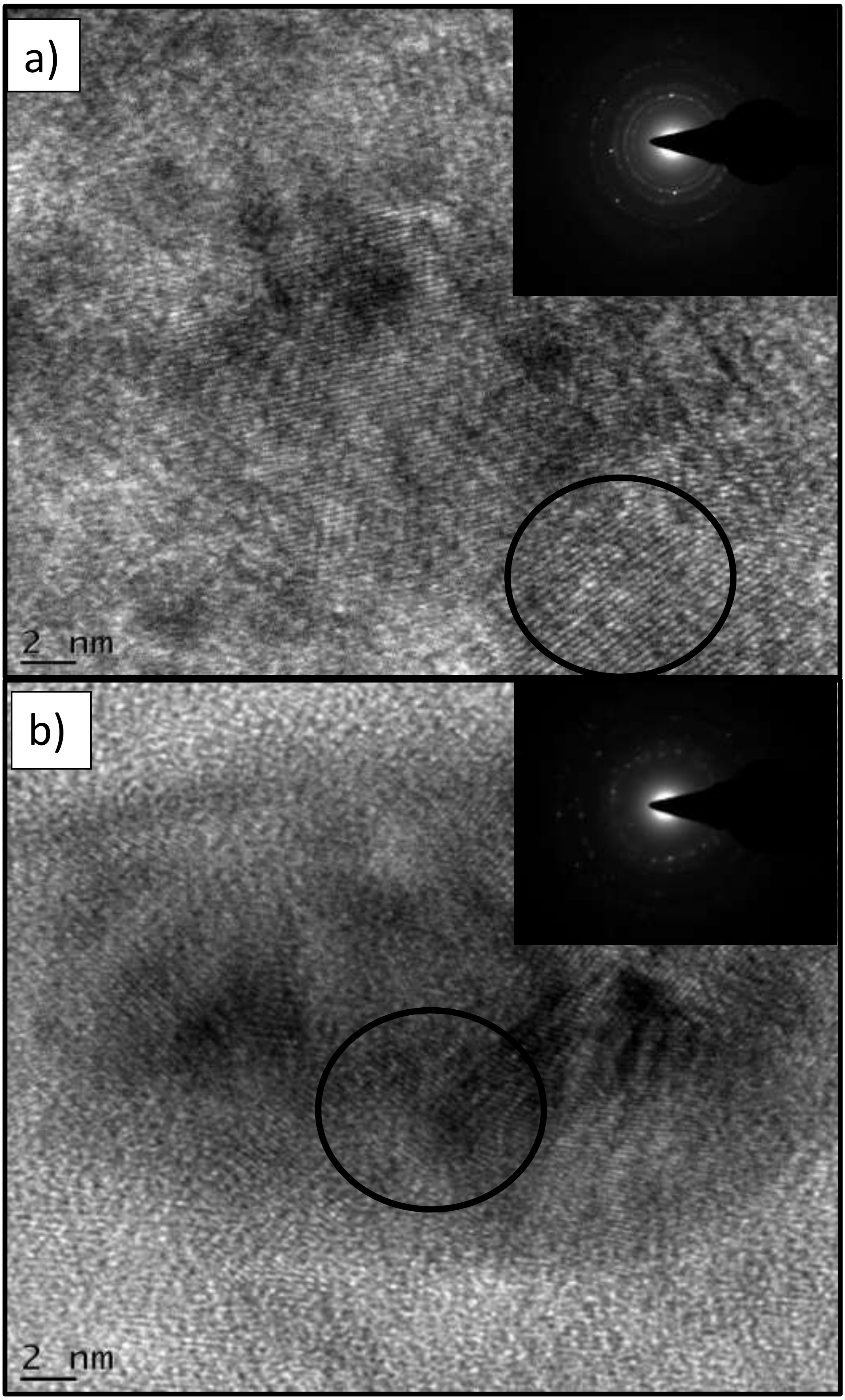

Figure 17: HRTEM image of a) Fe nanoparticles and b) AgFe nanoalloy both with inserts of SAED images.

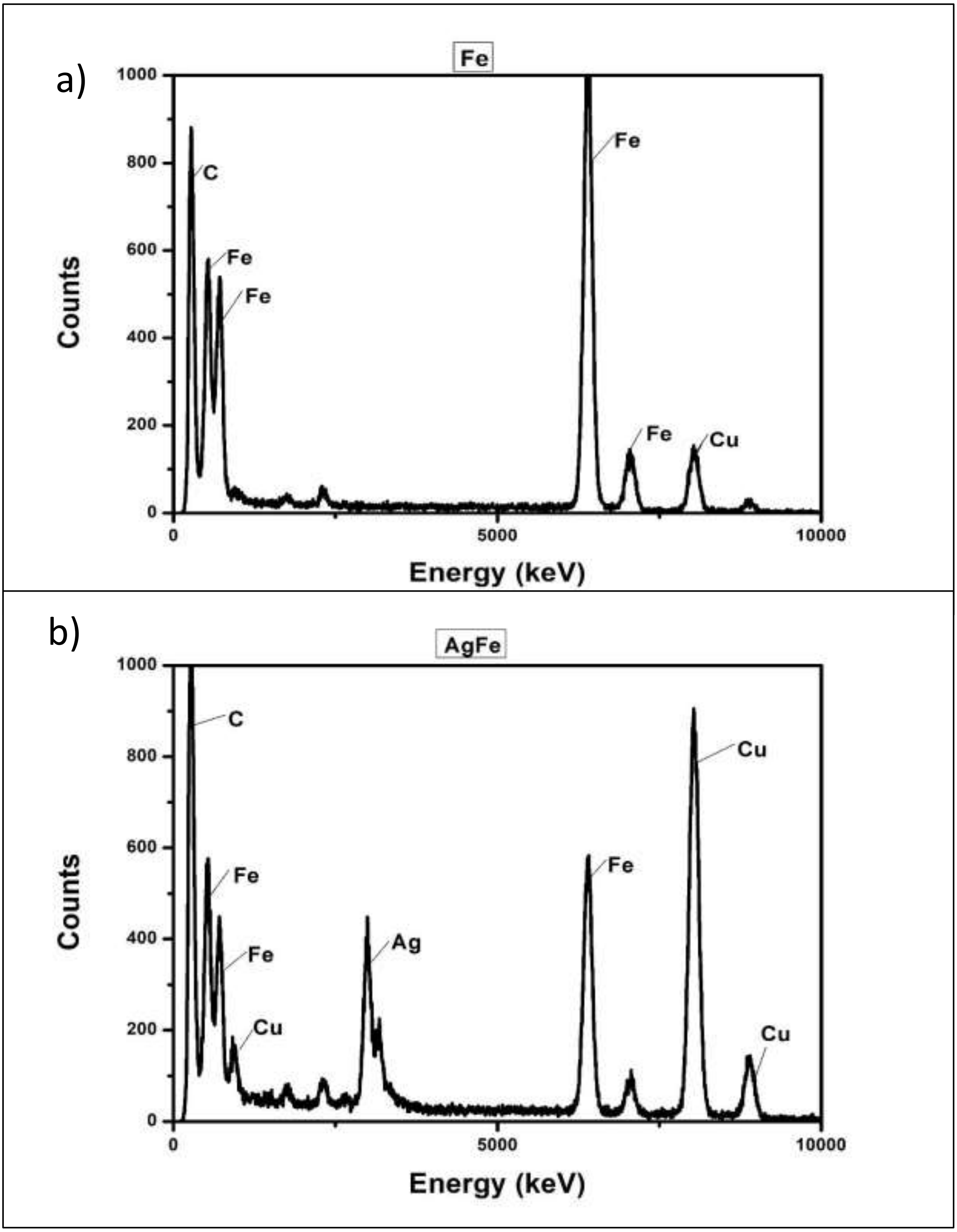

Figure 18: EDS graphs of a) Iron nanoparticles and b) AgFe nanoalloy.

Figure 16 and 17 shows the HRTEM images of TiO_2 degussa, a) Fe nanoparticles and b) AgFe nanoalloy respectively. For TiO_2 there are clear signs of lattice fringes confirming the crystallinity of the compound. The insert is a zoomed out HRTEM image of TiO_2 that can be seen to be made up of aggregated spherical shapes of TiO_2 into what looks like broad randomly shaped sheet-like structures. In Figure 17 a) and b) shows the clear lattice fringes (this was pointed out with circles) indicating the formation of crystallinity for Fe nanoparticles and AgFe nanoalloy respectively. The SAED insert with clear circular rings in image a) for Fe nanoparticles proved as confirmation of the vivid lattice fringes and thereby the crystalline structure of the Fe nanoparticles. The SAED insert with poor-fashioned circular rings in image b) for AgFe nanoalloy corresponds to the image b) where there are lattice fringes that are not as prominent as those for Fe nanoparticles in image a). This is an indication of decrease in consistency in the crystalline structure from that of Fe nanoparticles compared to when it is combined with Ag in the AgFe nanoalloy. This illustrates the effect Ag has on the Fe when combined as a nanoalloy to form AgFe. Figure 18 shows the EDS graphs for a) Fe nanoparticles and b) AgFe nanoalloy. In figure 18 a) there are four main peaks for Fe which serves as elemental confirmation that the sample does contain Fe. There are two other peaks namely carbon and copper, this is due to the carbon copper grid used for HRTEM sample analysis. In b) the EDS spectrum indicates that the sample is composed of Ag since there is a strong peak for Ag as well as Fe, as there are three peaks for Fe. The other three peaks are of carbon and copper which is due to the HRTEM grid used for analysis of the sample.

4.3 FTIR (Fourier Transform Infrared Spectroscopy)

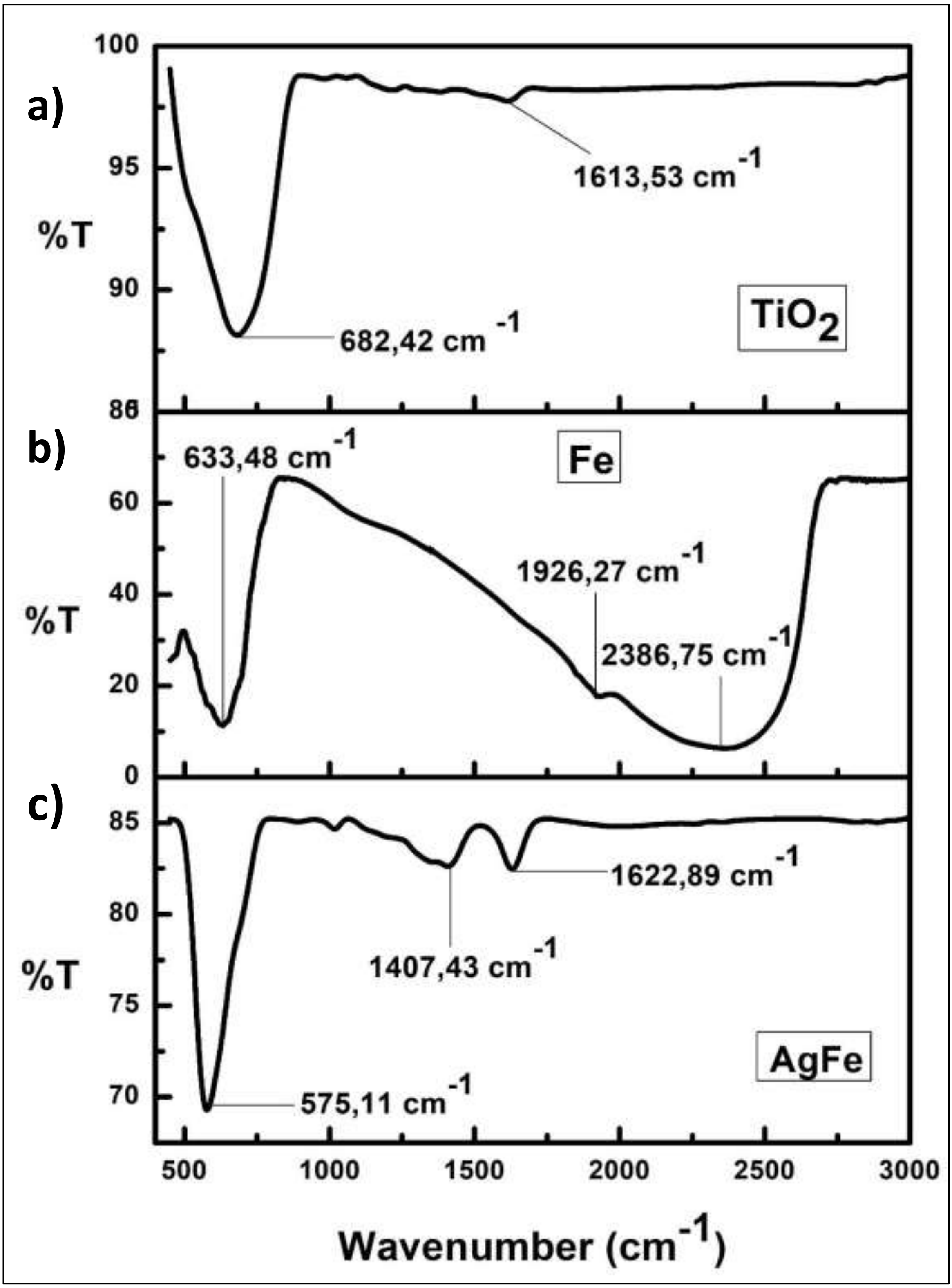

Figure 19: FTIR Spectra for a) TiO_2 degussa, b) Fe nanoparticles and c) AgFe nanoalloy

Figure 19 shows the FTIR spectra of a) TiO_2 degussa, b) Fe nanoparticles and c) AgFe nanoalloy. In Figure 19 a) shows a sharp band in the range 500 cm^{-1} -1000 cm^{-1} 6 due to the bending vibration of Ti-O-Ti bonds in the TiO_2 lattice similar to that found by researchers Al-Taweel, Saja S., and Haider R. Saud in 2016 . The same range (500 cm^{-1} -1000 cm^{-1}) also illustrates the bending of Ti-O and O-Ti-O according to the TiO_2 lattice. The band at 1613.53 cm^{-1} is due to the characteristic bending vibration of –OH group which correlates to the same range as one found by researchers Al-Taweel, Saja S., and Haider R. Saud in 2016. Figure 19 FTIR spectra b) shows an absorption band at 633.48 cm^{-1}, this is due to the Fe-O bonds according to researchers Sharma, Geetu, and Pethaiyan Jeevanandam in 2013. The absorption bands at 1926.27 cm^{-1} and 2386.75 cm^{-1} are in the same range as the bands found by Sharma, Geetu, and Pethaiyan Jeevanandam in 2013 who reported that the cause of this was due to O-H bending and stretching. The broad band of O-H stretching could be due to the instability of Fe at room temperature. In Figure 19 the FTIR spectra for c) shows a band at 575.11 cm^{-1} which is in a similar range to that reported previously by Sharma, Geetu, and Pethaiyan Jeevanandam in 2013 where this was said to be due to the Fe-O bonds. This confirms the presence of Fe in the nanoalloy AgFe. What is observed is that from Fe to AgFe the band in the range of 500 cm^{-1} – 1000 cm^{-1} becomes sharper which could be an indication of an increase in Fe nanoparticles. What can also be observed in figure 19 is that there is a decrease in the band in b) responsible for OH in the spectrum for Fe in spectrum c) of AgFe which implies that there was evaporation of water molecules since heat was applied during the synthesis of AgFe, but instead what can be observed is the creation of two small peaks in the range of 900 cm^{-1}-1750 cm^{-1}, this is due to the silver.

4.4 UV-vis (Ultraviolet-visible spectroscopy)

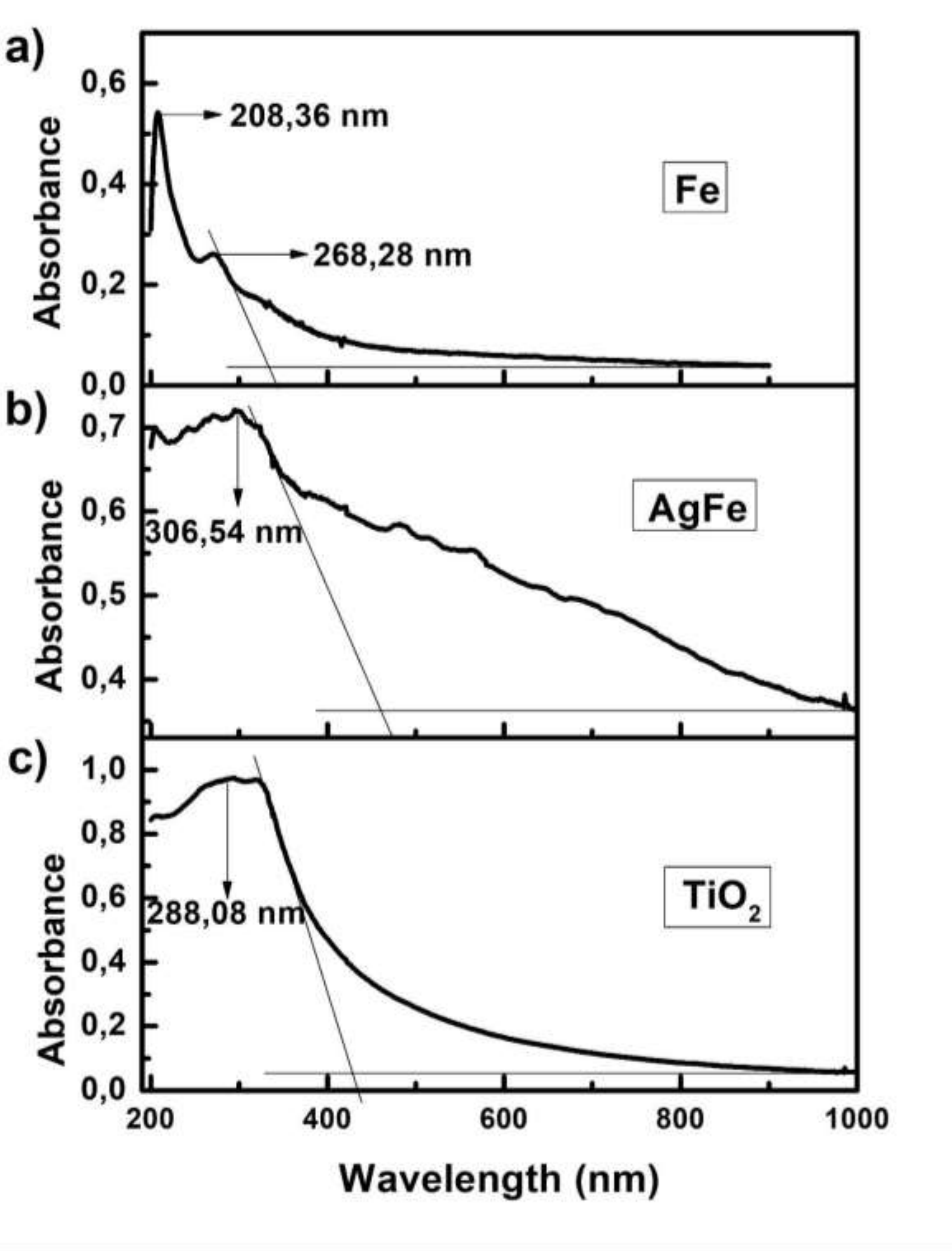

Figure 20: UV-Vis spectra for a) Fe Nanoparticles, b) AgFe nanalloy and c) TiO_2 degussa

Figure 20 shows the UV spectra of a) Fe nanoparticles, b) AgFe nanoalloy and c) TiO_2 degussa. In Figure 20 a) shows a sharp absorption peak at in the range of 200 nm to 300 nm similar to that found by Paul Raj, Samuel in 2013 and is said to prove the presence of Fe nanoparticles. The band gap for the synthesised Fe nanoparticles was calculated using the onset in the graph and the formula E = $\frac{hC}{\lambda}$. It was therefore found that the band gap for Fe nanoparticles was 3.73 eV. Figure 20 b) AgFe shows an onset and the wavelength was used to calculate the band gap of 2.5 eV. This is an indication that the nanoalloy AgFe has a smaller band gap then that of Fe nanoparticles which therefore means that the band gap was improved in the nanoalloy. In figure 20 c) the band gap for TiO_2 degussa was calculated to be 2.93 eV. This is close to the standard band gap of TiO_2 degussa which is normally 3.1 eV. The lower band gap for the TiO_2 degussa is due to the fact that it is in the form of a nanopowder (this increases the surface area). Since the band gap of AgFe was calculated to be 2.5 eV it can be said that it should lower the band gap of the TiO_2 and cause a right shift (red shift) of the TiO_2 peak.

4.5 XRD (X-ray diffraction)

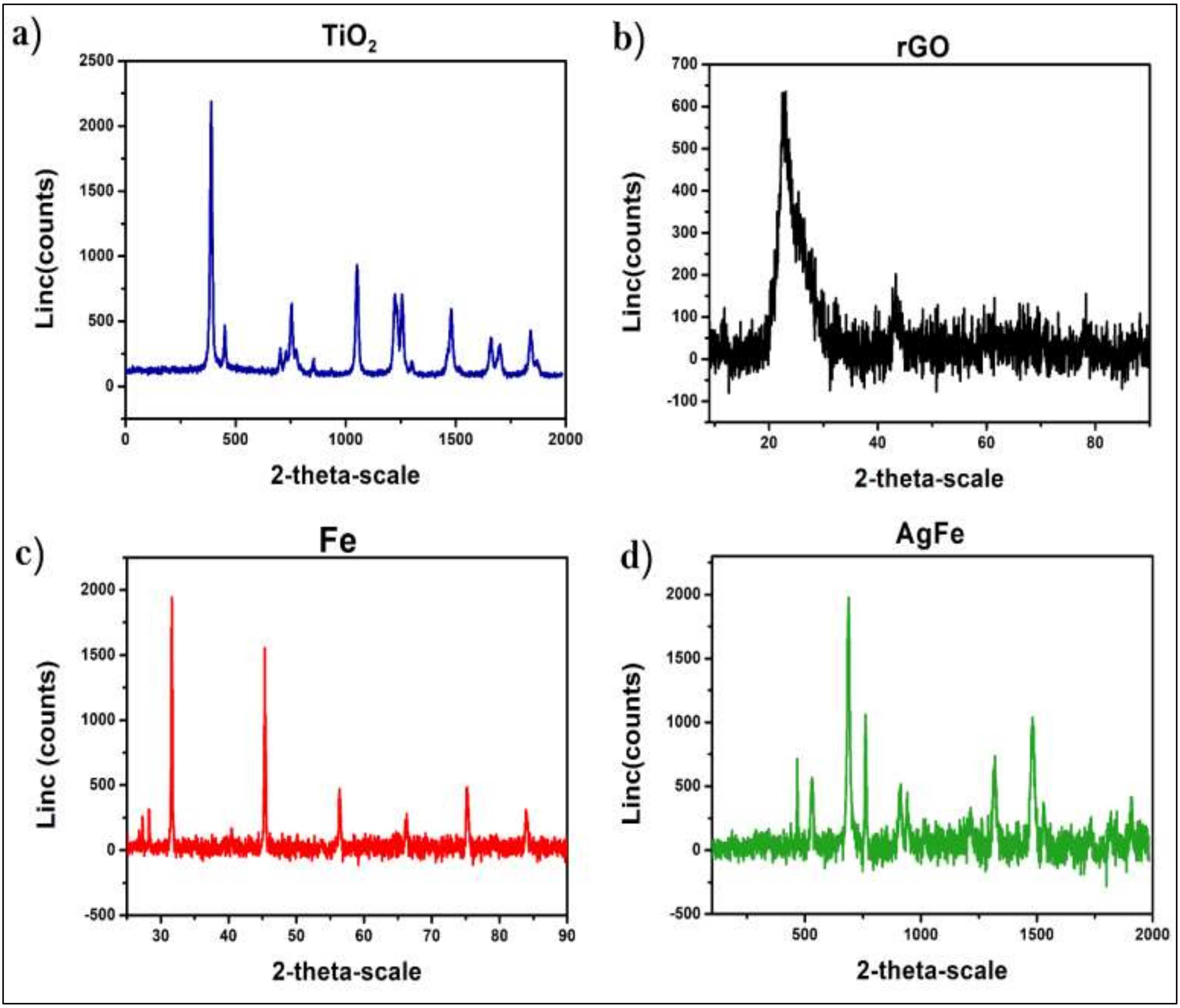

Figure 21: X-ray diffraction (XRD) patterns of the samples a) TiO_2 degussa, b) reduced graphene oxide, c) Fe and d) AgFe.

Figure 21 shows the XRD patterns of a) TiO_2 degussa indicates that the TiO_2 degussa is in anatase phase as highest peaks correlate with that of TiO_2 anatase, also the amount of peaks serve as an indication of the samples crystallinity. This correlates with the TEM image of TiO_2 degussa in figure 16. Figure 21 also shows the XRD patterns of rGO (reduced graphene oxide) which indicates that the sample is amorphous and this expected for rGO as it speaks to the lack of crystallinity of the sample. The XRD patterns for Fe nanoparticles observed in c) suggest and correlate with that of Fe nanoparticles in literature. The patterns also indicate that there is a high degree of crystallinity which confirms/correlates with the findings in figure 17 a) which shows a TEM image of Fe nanoparticles. The XRD for d) AgFe nanoalloy indicates that the sample is crystalline as observed in TEM image of AgFe (Figure 17 b). The peaks in figure 21 d) are an indication of both Ag and Fe in the forms 3C and magnatite respectively according to the XRD analysis. The XRD analysis also indicated that there is a slight overlap of the Ag patterns and TiO_2 therefore there are similar peaks in Figure 21 a) and d). The calculated d-spacing for the base photocatalyst was 3.08 nm which is in accordance with that of the XRD TiO_2 nanoparticle research carried out by Theivasanthi et al.

4.6. CV (Cyclic voltammetry)

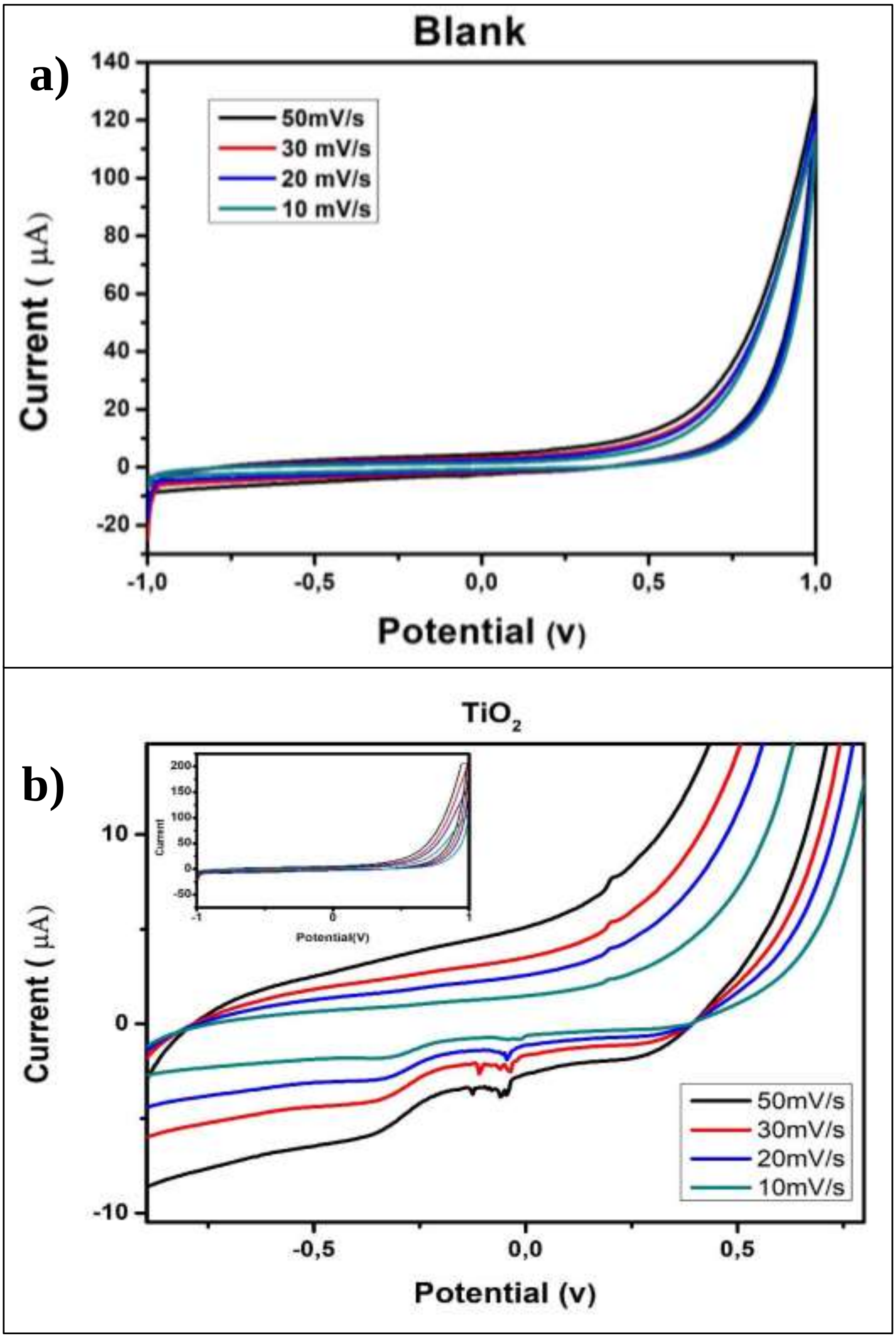

Figure 22: CV graph of a) Blank of glassy carbon electrode in 5M LiOH electrolyte at scan rates 10 mV/s, 20 mV/s, 30 mV/s, 50 mV/ b) 100 mg TiO$_2$ degussa of scan rates 10 mV/s, 20 mV/s, 30 mV/s, 50 mV/s in 5M LiOH electrolyte with insert on a glassy carbon electrode.

Scan Rate ($mV.s^{-1}$)	Scan Rate$^{1/2}$ ($mV.s^{-1}$)	Ipc (μA)	Ipa (μA)	Epa (V)	Epc (V)	ΔEp (V)
10	3.16	-0.630	0.630	0.200	-0.050	0.250
20	4.47	-0.900	0.968	0.202	-0.042	0.244
30	5.48	-0.834	1.260	0.200	-0.046	0.246
50	6.32	-1.12	1.808	0.202	-0.042	0.244
Mean		**0.855**	**1.17**	**0.201**	**-0.045**	**0.246**

Table 1: Scan rate vs Scan Rate$^{1/2}$ ($mV.s^{-1}$) vs Ipc, Ipa, Epa and Epc

Determination of reversibility:

$$\frac{\mathbf{Ipa}}{\mathbf{Ipc}} = \frac{\mathbf{1.17\ \mu}\boldsymbol{A}}{\mathbf{0.855\ \mu}\boldsymbol{A}}$$

$$= \mathbf{1.37\ \mu}\boldsymbol{A}$$

$$\therefore -\frac{\boldsymbol{Ipa}}{\boldsymbol{Ipc}} \approx \mathbf{1} \ldots \boldsymbol{Chemically\ reversible}$$

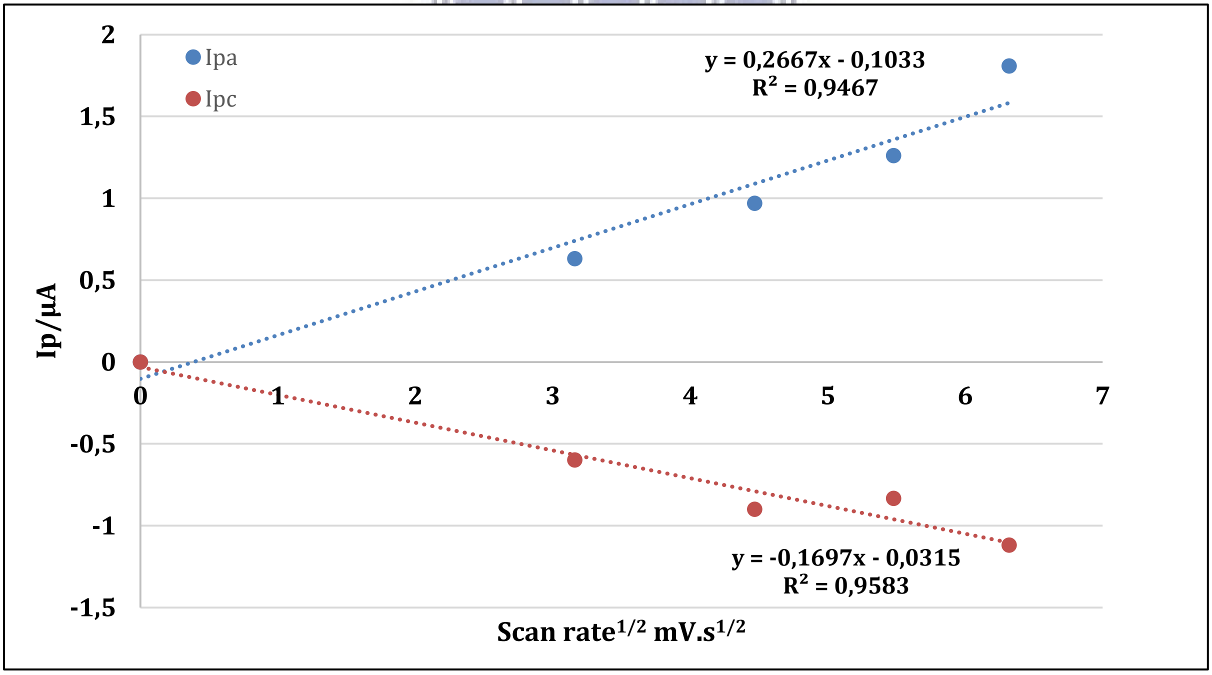

Figure 23: Plot of peak current vs root squared

Determination of Diffusion Coefficient:

$$D^{1/2} = \frac{j_p}{2.72 \times 10^5 \times n^{3/2} \times A \times C_0 \nu^{1/2}},$$

$$D^{1/2}{}_{(TiO_2)} = \frac{\frac{20.56\ A}{m^2}}{2.72 \text{ x } 10^5 \times 1^{\frac{3}{2}} \times 0.071\ m^2 \times 5\ M \times 0.05^{\frac{1}{2}}}$$

$$D^{1/2}{}_{(TiO_2)} = 9.522 \text{ x } 10^{-4}$$

$$D_{(TiO_2)} = 9.07 \text{ x } 10^{-7} \text{ cm}^2.\text{s}^{-1}$$

Figure 22 shows the Cyclic voltammetric graph of a) blank and b) TiO_2 degussa at different scan rates with insert. The insert in b) is the zoomed out image of the CV graph and does not display any peaks however compared to the blank its current had increased with each increase in scan rate, with 50 mV/s having the highest current peak. Since the zoomed out image (Figure 22 b) insert) of the CV graph did not display any peaks it was zoomed in to observe possible peaks and shows one oxidation (anodic) peak of average peak 1.17 eV. It also contains a reduction (cathodic) peak of average 0.85 eV. What can also be observed is the increase peaks in graph b) TiO_2 degussa with an increase in scan rate. The electrochemical behaviour, as it presents itself here, is in accordance with the unique structural aspects of TiO2, it shows to be equivalent to a diffusion process. On the subject of scan rates and electron transfer, as the scan rate increased, a marked negative shift in peak potentials could be observed. This suggests the onset of limiting kinetic effects in association with increase in scan rate. Using $\frac{\mathbf{Ipa}}{\mathbf{Ipc}}$ the reaction proved to be reversible and the diffusion coefficient was calculated to be 9.07 x 10^{-7} $cm^2.s^{-1}$.

Chapter 5 (Results and discussion - Composites)

5.1 HRSEM (High resolution Scanning Electron Microscopy)

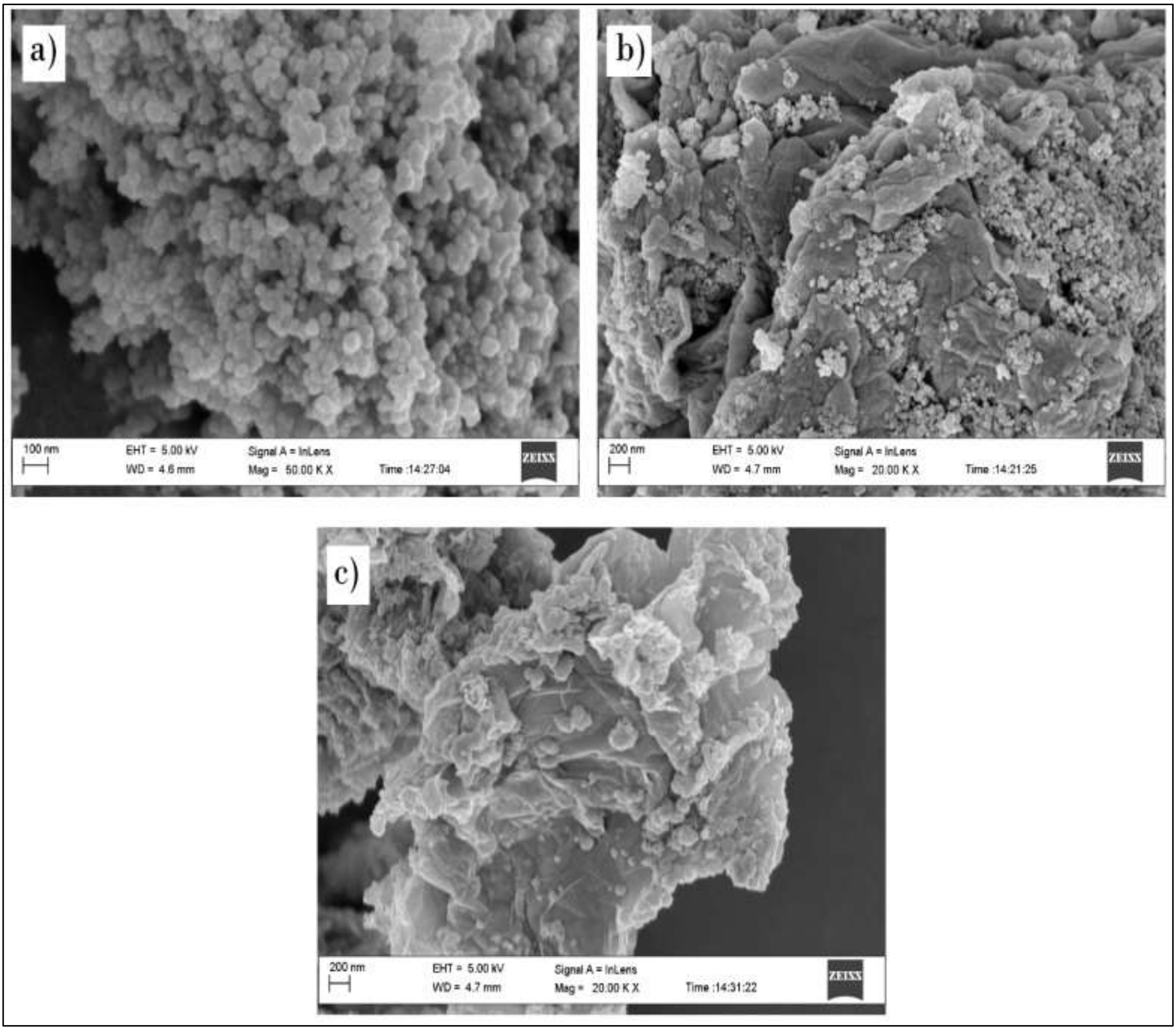

Figure 24: SEM images of a) AgFe- TiO_2, b) rGO-AgFe-TiO_2 and c) AgFe-rGO nanocomposites where a) is at a magnitude of 20.00 K X and b) and c) is at a magnitude of 50.00 K X.

Figure 24 shows SEM image a) AgFe-TiO_2. This can be seen similar to that of the TiO_2 degussa and AgFe where you find agglomerations of spherical shapes and some particles are less clustered then others. Figure 24 b) shows the SEM image of rGO-AgFe-TiO_2 where both the AgFe and the TiO_2 is seen to be intertwined with the rGO sheet-like structures. These sheet-like structures have allowed for the creation of pockets that may act as a hiding place for molecules during photocatalysis. In Figure 24 b) there are agglomerated particle structures that are lighter than others and this is an indication of the difference between the TiO_2 and AgFe nanoparticles. Figure 24 c) shows the SEM image of the nanocomposite AgFe-rGO. The image shows the sheet-like nature of the rGO and attached are small clusters of AgFe nanoalloy (this is seen as crumbs on the surface of the r-GO). What is evident in this image (Figure 24 c) is the brightness of those clusters. In Figure 24 a) it can be seen that there is more free space in terms of interaction during photosynthesis and this stems from the greater surface area compared to that of image b) and c) (Figure 24) where the sheet-like structures contribute to the possible hindrance in terms of its interaction with the water contaminant during photocatalysis. It is therefore speculated that photocatalysis would be carried out more efficiently with the AgFe-TiO_2 (image a).

The composition of each of the nanocomposites in Figure 21 AgFe-TiO_2, AgFe-rGO and AgFe-TiO_2-rGO was determined using EDS via SEM to confirm the elemental composition of each of the nanocomposites. This can be seen in Table 2

Element	**Atomic Percentage (%)**		
	AgFe-TiO_2	**AgFe-rGO**	**AgFe-TiO_2-rGO**
O	64.67	33.63	36.60
Ti	31.86	-	14.50
Fe	0.85	8.92	7.24
Ag	2.62	5.39	5.72
C	-	52.06	35.94
Total	100		

Table 2: Table representing the percentage elemental composition of the nanocomposites AgFe-TiO_2, AgFe-rGO and AgFe-TiO_2-rGO.

Table 1 represents the elemental composition percentages of the nanocomposites as confirmation for the various elements in those specific nanocomposites. For the Nanocomposite AgFe-TiO_2, oxygen has the greatest percentage (64.67 %) composition due to the TiO_2 molecule, where there are two oxygens for every Titanium atom (31.86 %). According to the table this nanocomposite (AgFe-TiO_2) contains 0.85 % Iron and 2.62 % Silver therefore indicating that the AgFe nanoalloy contains a greater percentage of silver. For the Nanocomposite AgFe-rGO the greatest percentage (52.06 %) is Carbon, which is due to the rGO and the oxygen then follows with 33.63% which also contributes to the composition of rGO. The difference between AgFe-rGO and AgFe-TiO_2 in terms of AgFe is the ratio of silver to Iron, according to the table, since the percentage of Iron is greater (8.92 %) than silver (5.39 %) in the nanocomposite AgFe-rGO compared to AgFe-TiO_2 where silver has a larger percentage than Iron. AgFe-TiO_2-rGO has an elemental composition of 36.60% for oxygen which is slightly larger than carbon (35.94 %). This is due to the oxygen in TiO_2, where there is a balance of two oxygen atoms per titanium (14.50 %) atom, approximately leaving an “extra” 17.61% of oxygen atoms that could be due to rGO. AgFe-TiO_2-rGO does experience the same Iron favoured ratio with an atomic percentage of 7.24 % and less so for silver having an atomic percentage of 5.72 %. These values have a significant impact on photocatalysis.

5.2 FTIR (Fourier Transform Infrared Spectroscopy)

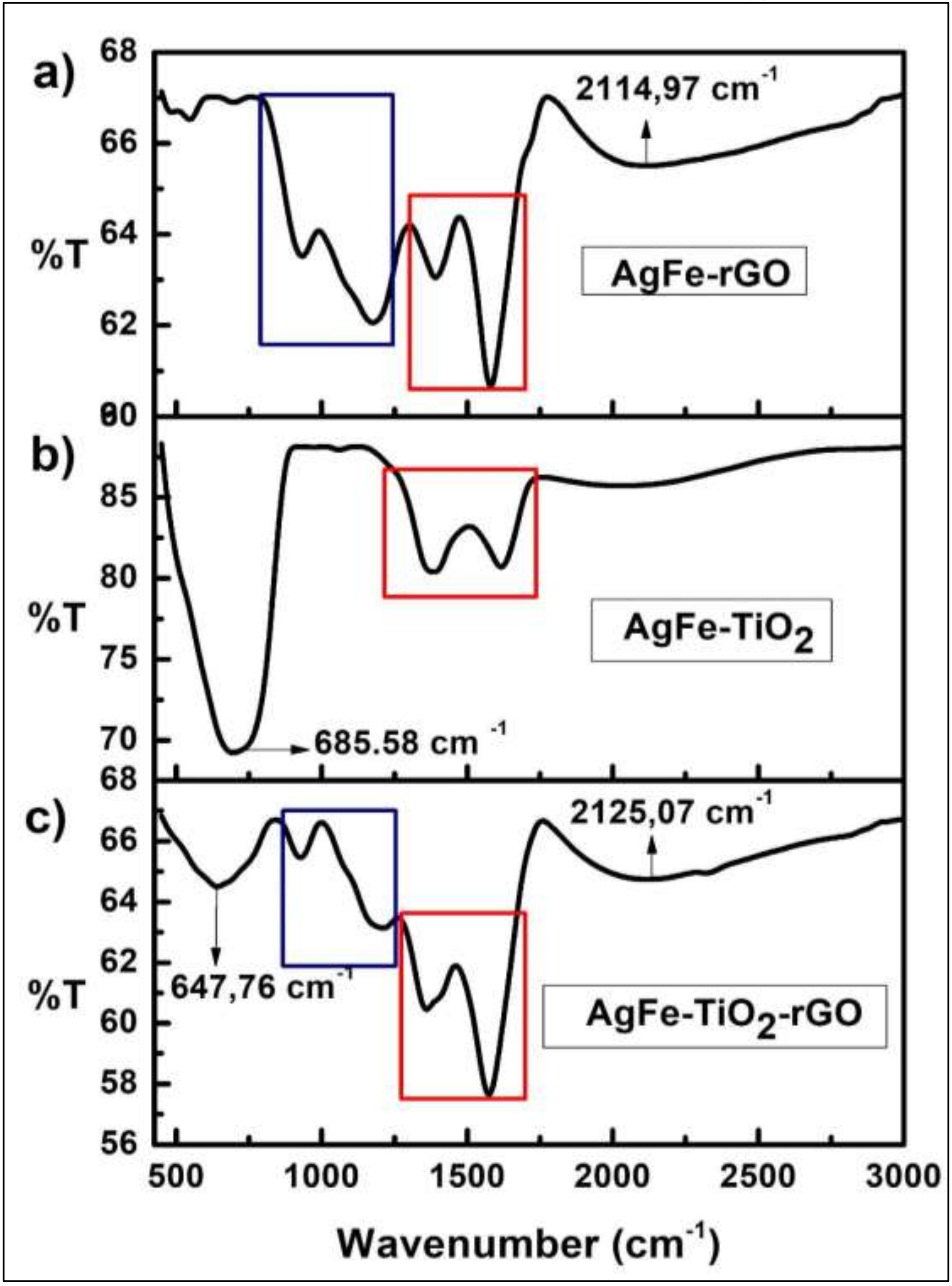

Figure 25: FTIR Spectra for nanocomposites a) AgFe-rGO, b) AgFe-TiO_2 and c) AgFe-TiO_2-rGO.

Figure 25 presents the FTIR spectra for a) AgFe-rGO where a clear band is seen from about 1800 cm^{-1} to 2900 cm^{-1} caused by the O-H bending and stretching and this is like-wise illustrated in spectrum c) (AgFe-TiO_2-rGO) therefore confirming the origin of this band to be stemmed from rGO. Spectrum a) contains a blue box inset encapsuling the band ranging from 850 cm $^{-1}$ to 1260 cm^{-1} and is evident in the blue box shown in spectrum c) AgFe-TiO_2-rGO. Therefore both Spectrum a) and c) is an indication of C-C bending and stretching corresponding to the rGO since graphene is made up of carbon. Figure 25 spectrum a) also contains a red box highlighting the band of range 1250 cm^{-1} to about 1765 cm^{-1}. This red box is observed in all three spectra which all contain AgFe, therefore concluding that this band is due to AgFe in all three nanocomposites. In spectra a), b) and c) the red box contains two bands, the one the right is roughly at 1625 cm^{-1} which is due to the Fe-O bending and stretching as an indication of Fe in the nanocomposite. However in both spectra a) and c) this band is sharper than that of spectra b), this could therefore be due to the larger atomic percentage of Fe in both AgFe-rGO and AgFe-TiO_2-rGO compared to AgFe-TiO_2. Conversely the red box in spectrum b) contains shorter bands and the band on the left at 1370 cm^{-1} (the same band in all three spectra) is sharper than that of its neighbour (at 1625 cm^{-1}, owned by Fe). This in relation to Table 1 is quite possibly due to the larger atomic percentage of Ag compared to Fe in AgFe-TiO_2. Spectrum b) and c) contains a band of range 500 cm^{-1} to 900 cm^{-1} which is due to the bending vibration of Ti-O-Ti, O-Ti-O and Ti-O bonds in the TiO_2 lattice. In spectrum b) this band (500 – 900 cm $^{-1}$) is significantly longer than that in spectrum c) which corresponds with the findings in Table 1 where there is a greater percentage of TiO_2 (Ti and O) in AgFe-TiO_2 than in AgFe-TiO_2-rGO.

5.3 UV-vis (Ultraviolet-visible spectroscopy)

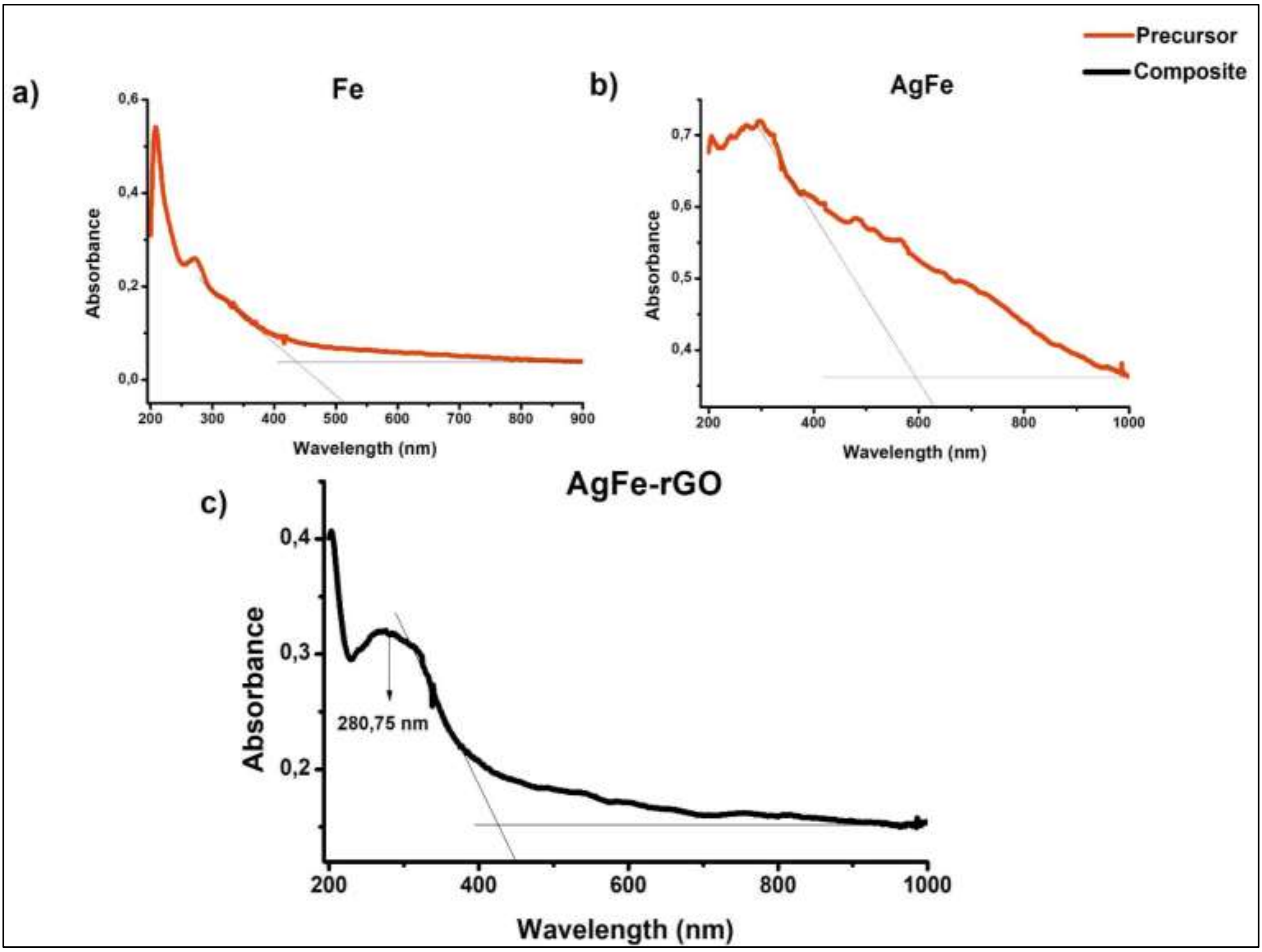

Figure 26: UV-vis spectra for the precursors a) Fe nanoparticles,b) AgFe nanoalloy and nanocomposite c) AgFe-rGO each with onset.

Figure 26 shows the UV-vis spectra for the nanocomposite AgFe-rGO which has a slightly broad peak at 280.75 nm similar to that of the precursor AgFe (spectrum b) which has a peak in the same range as 280.75 nm. This specific range is between 200 nm and 400 nm which is the same range as the absorbance peak for rGO as a result of the π-π transitions of the aromatic C-C bonds. The band gap for the nanocomposite AgFe-rGO was calculated using the onset in

Figure 26 spectrum c) and the formula E = $\frac{hC}{\lambda}$. The band gap for AgFe-rGO was therefore calculated to be 2.97 eV. This is smaller than the previously calculated band gap of Fe (3.73eV) and larger than the band gap of AgFe (2.5eV). This is an indication that the AgFe-rGO may prove to decrease the photocatalytic ability of TiO_2 in the nanocomposite AgFe-TiO_2-rGO.

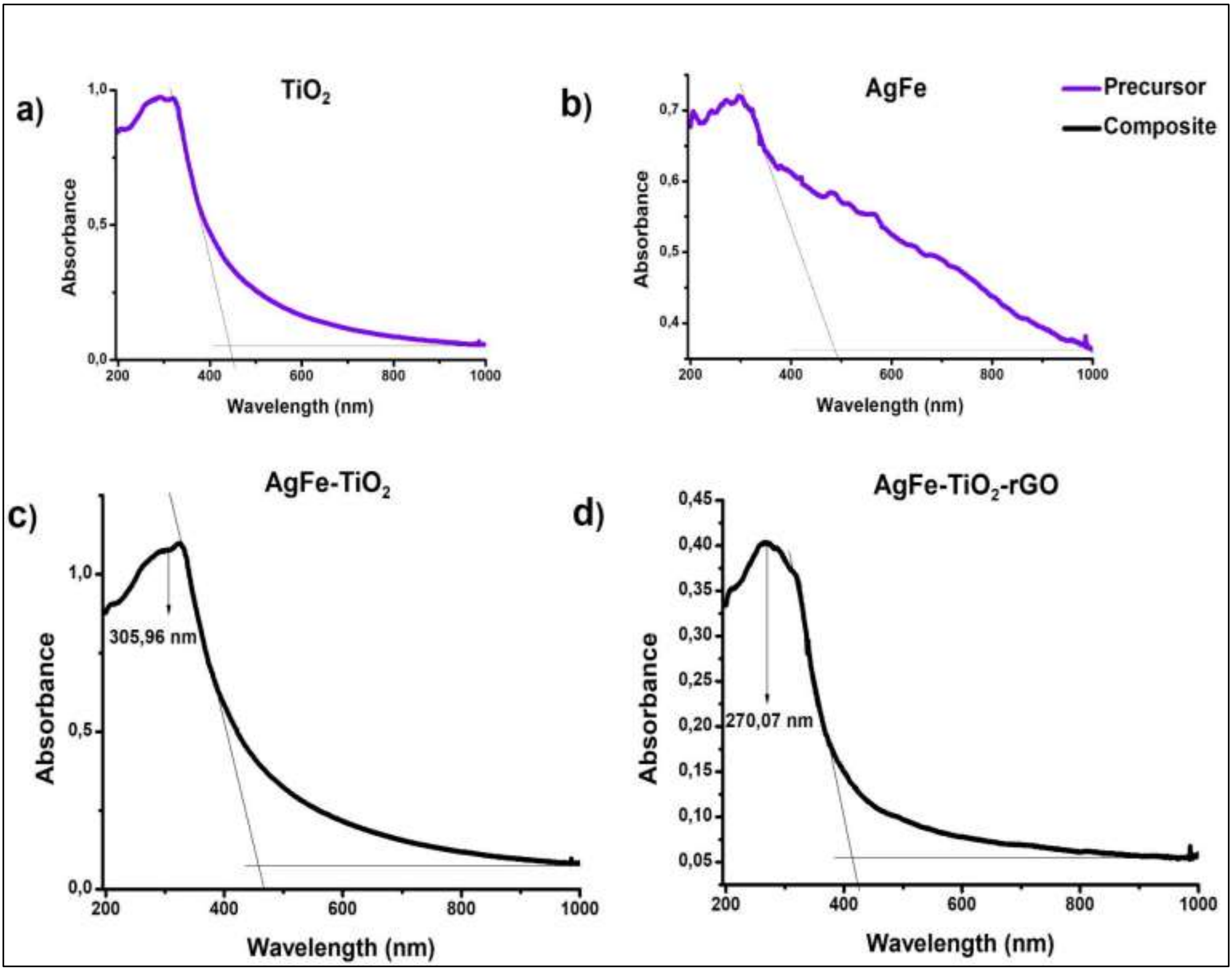

Figure 27: UV-vis spectra for the precursors a) TiO_2 (Degussa),b) AgFe nanoalloy , nanocomposites c) AgFe-TiO_2 and d) AgFe-TiO_2-rGO each with onset.

Figure 27 shows the UV-vis spectra for the nanocomposites c) AgFe-TiO_2 and d) AgFe-TiO_2-rGO. In Figure 27 c) there is a peak that is in the same range (200 nm – 400 nm) as that of the peak for the a) TiO_2 precursor, however the difference is the ultimately the very slight shift in the peak (shift to the right/ which is essentially a red shift) of c) AgFe-TiO_2, this correlates with the band gap which was calculated to be 2.77 eV. For figure 27 d) the same is evident compared to c) where the peak occurs in the same range (200 nm – 400 nm) as a) TiO_2 precursor, however it displays a slight shift (to the left/a blue shift) of the peak, this correlates with the band gap which was calculated to be 3.02 eV. This therefore means that the b) AgFe (with a band gap of 2.5 eV) has caused the improvement of the photocatalytic reactivity of a) TiO_2, however that the rGO seems to have worked against the b) AgFe nanoalloy since it increased the band gap tremendously.

5.4 XRD (X-ray Diffraction)

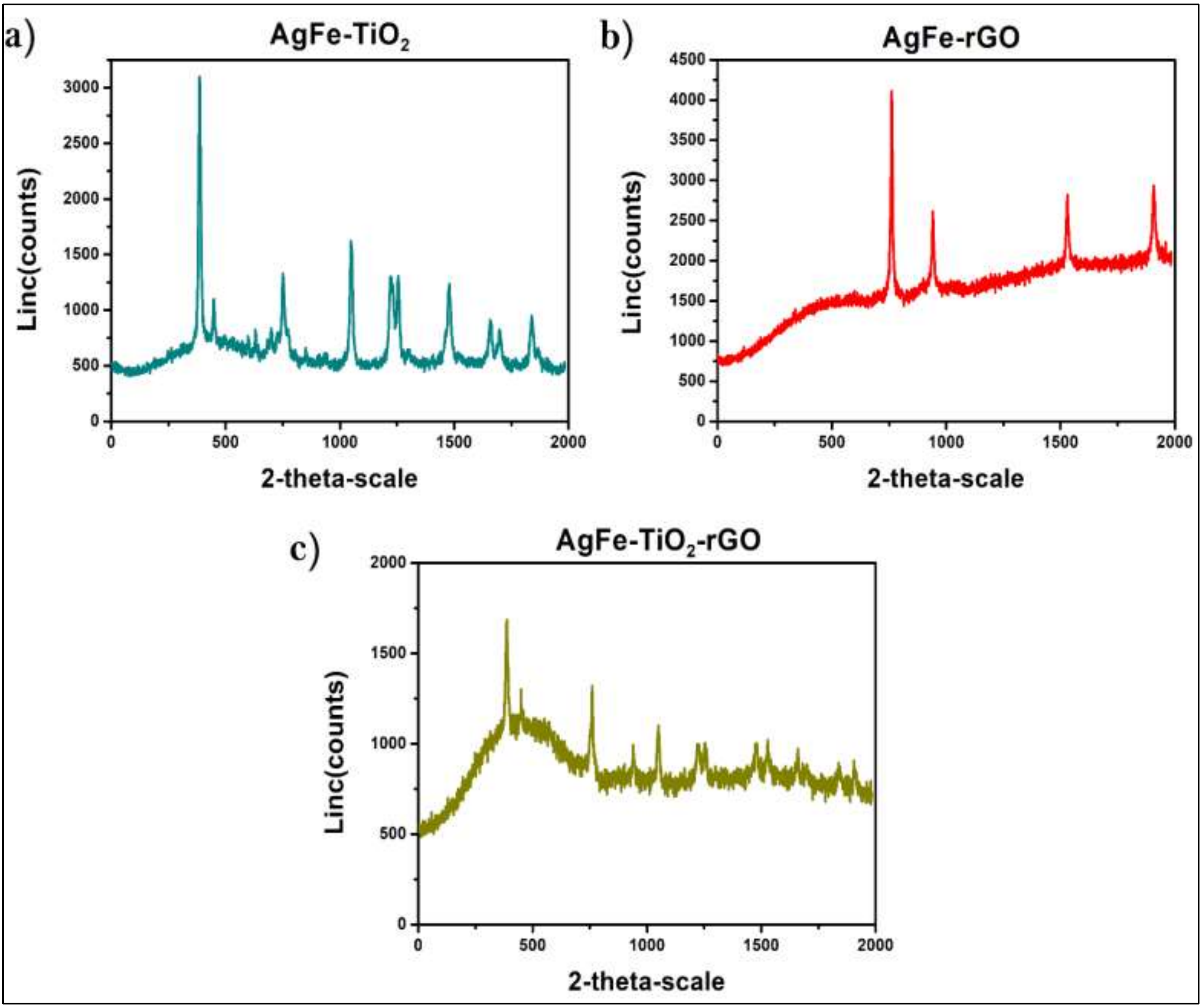

Figure 28: X-ray diffraction (XRD) patterns of the nanomposite samples a) AgFe-TiO_2, b) AgFe-rGO and c) AgFe-TiO_2-rGO.

Figure 28 shows the XRD patterns of a) AgFe-TiO_2 and according to the analysis the composite contains both Ag and Fe similar to that of patterns found in figure 21 a) and d) which show the XRD patterns of TiO_2 degussa and AgFe respectively. Therefore this also confirms the crystallinity of the composite. The XRD patterns in Figure 28 c) AgFe-TiO_2-rGO are similar to that found in Figure 28 a) AgFe-TiO_2 which therefore confirms the presence of Ag, Fe and TiO_2. However the peaks are observed to be sharper in Figure 28 a) AgFe-TiO_2 compared to that of the peaks in c) AgFe-TiO_2-rGO and since the crystallinity of a) AgFe-TiO_2 is confirmed through the peaks the crystallinity is somewhat challenged in the composite c) AgFe-TiO_2-rGO where you can see a broad peak in the results around 500(2-theta-scale), and this is due to the reduced graphene oxide (rGO). This same effect is seen in the composite b) AgFe-rGO where the same broad peak is seen at 500(2-theta-scale). What is also seen in b) AgFe-rGO is the slight shift in peaks to the right and the XRD analysis indicate that there are peaks confirming the presence of Ag and Fe although very slight. The d-spacing for AgFe-TiO_2 and AgFe-TiO_2-rGO was calculated to be 2.22 nm and 3.25 nm respectively.

5.5 CV (Cyclic voltammetry)

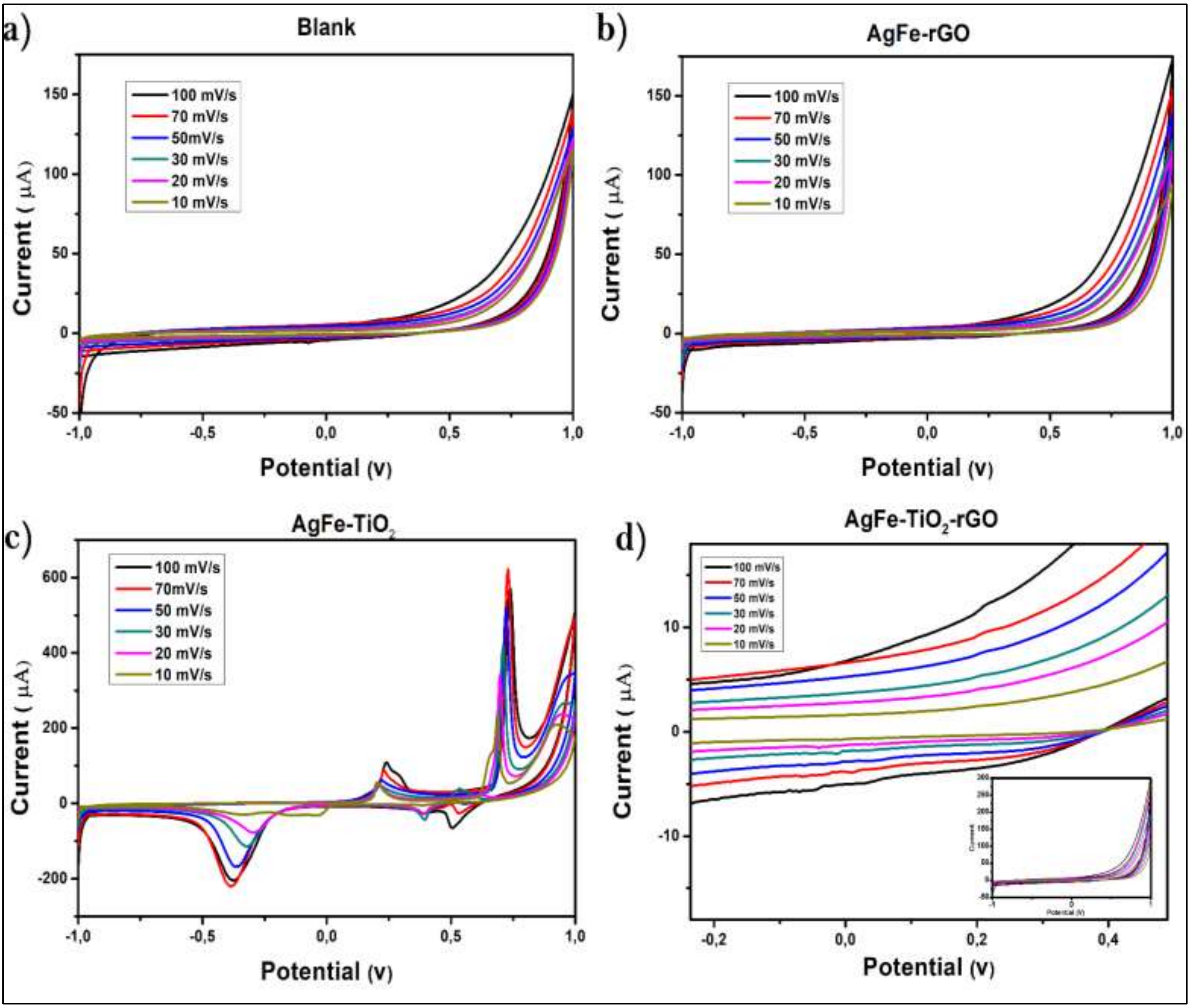

Figure 29: CV graph of a) Blank of glassy carbon electrode, nanocomposites b) 100 mg AgFe-rGO, c) 100 mg AgFe- TiO_2 and d) 100 mg AgFe-TiO_2-rGO with insert in 5M LiOH electrolyte at scan rates 10 mV/s, 20 mV/s, 30 mV/s, 50 mV/ s, 70 mV/s and 10 mV/s in 5M LiOH electrolyte on a glassy carbon electrode.

Scan Rate ($mV.s^{-1}$)	Scan Rate$^{1/2}$ ($mV.s^{-1}$)	Ipc (µA)	Ipa (µA)	Epa (V)	Epc (V)	ΔEp (V)
10	3.16	0.46	3.52	0.217	-0.054	0.271
20	4.47	0.61	3.52	0.213	-0.054	0.267
30	5.48	0.74	3.58	0.213	-0.052	0.265
50	6.32	1.06	6.58	0.215	-0.054	0.269
70	8.37	1.54	5.36	0.217	-0.052	0.269
100	10	1.98	8.73	0.215	-0.054	0.269
Mean		**1.07**	**5.22**	**0.215**	**-0.053**	**0.268**

Table 3: Scan rate vs Scan Rate$^{1/2}$ ($mV.s^{-1}$) vs Ipc, Ipa, Epa and Epc for AgFe-TiO_2-rGO

Determination of reversibility:

$$\frac{\mathbf{Ipa}}{\mathbf{Ipc}} = \frac{\mathbf{5.22\ \mu A}}{\mathbf{1.07\ \mu A}}$$

$$= \mathbf{4.88\ \mu A}$$

$$\therefore -\frac{Ipa}{Ipc} \not\approx \mathbf{1} \ldots \boldsymbol{therefore\ it\ is\ chemically\ irreversible}$$

Determination of Diffusion Coefficient:

$$D^{1/2} = \frac{j_p}{2.72 \times 10^5 \times n^{3/2} \times A \times C_0 \nu^{1/2}},$$

$$D^{1/2}{}_{(AgFe\text{-}TiO_2\text{-}rGO)} = \frac{\frac{150.85\ A}{m^2}}{2.72 \text{ x } 10^5 \times 1^{\frac{3}{2}} \times 0.071\ m^2 \times 5\ M \times 0.1^{\frac{1}{2}}}$$

$$D^{1/2}{}_{(AgFe\text{-}TiO_2\text{-}rGO)} = 4.94 \text{ x } 10^{-3}$$

$$D_{(AgFe\text{-}TiO_2\text{-}rGO)} = 2.44 \text{ x } 10^{-5}\ cm^2.s^{-1}$$

Scan Rate ($mV.s^{-1}$)	Scan $Rate^{1/2}$ ($mV.s^{-1}$)	Ipc (μA)	Ipa (μA)	Epa (V)	Epc (V)	ΔEp (V)
10	3.16	14.66	94.06	0.20	0.39	-0.19
20	4.47	199.18	92.17	0.20	0.39	-0.19
30	5.48	127.64	94.58	0.21	0.39	-0.18
50	6.32	131.7	96.72	0.21	0.39	-0.18
70	8.37	148.24	103.1	0.23	0.40	-0.17
100	10	153.09	145.53	0.24	0.39	-0.15
Mean		**129.10**	**104.3**	**0.22**	**0.39**	**-0.18**

Table 4: Scan rate vs Scan $Rate^{1/2}$ ($mV.s^{-1}$) vs vs Ipc, Ipa, Epa and Epc for $AgFe\text{-}TiO_2$

Determination of reversibility:

$$\frac{\mathbf{Ipa}}{\mathbf{Ipc}} = \frac{\mathbf{104}\ \mu\boldsymbol{A}}{\mathbf{129.10}\ \mu\boldsymbol{A}}$$

$$= \mathbf{0.81}\ \mu\boldsymbol{A}$$

$$\therefore -\frac{\boldsymbol{Ipa}}{\boldsymbol{Ipc}} \approx \mathbf{1} \ldots \boldsymbol{therefore\ it\ is\ chemically\ reversible}$$

Determination of Diffusion Coefficient:

$$D^{1/2} = \frac{j_p}{2.72 \times 10^5 \times n^{3/2} \times A \times C_0 \nu^{1/2}},$$

$$D^{1/2}{}_{(AgFe\text{-}TiO_2)} = \frac{\frac{149.31\ A}{m^2}}{2.72 \text{ x } 10^5 \times 1^{\frac{3}{2}} \times 0.071\ m^2 \times 5\ M \times 0.1^{\frac{1}{2}}}$$

$$D^{1/2}{}_{(AgFe\text{-}TiO_2)} = 4.89 \text{ x } 10^{-3}\ 2.25 \text{ x } 10^{-3}$$

$$D_{(AgFe\text{-}TiO_2)} = 2.39 \text{ x } 10^{-5}\ cm^2.s^{-1}$$

Figure 29 shows CV graph for a) Blank of glassy carbon electrode, nanocomposites b) AgFe-rGO, c) AgFe- TiO_2 and d) AgFe-TiO_2-rGO with insert. Figure 29 b) AgFe-rGO doesn't display any peaks, however compared to a) blank there is an increase in current with increase in scan rates where 100 mV/s has the highest current in b). Figure 29 c) displays two oxidation (anodic) peaks and two reduction (cathodic) peaks and this is due to the oxidation states of Fe. What is also observed (Figure 29 c) is the increase in peak current with increase in scan rate with 100 mV/s having the highest peaks for both oxidation and reduction. Figure 29 d) AgFe-TiO_2-rGO has an insert that is zoomed out CV graph of AgFe-TiO_2-rGO and when compared to a) shows no peaks but does display an increase in current with increase in scan rate, with the 100 mV/s having the highest current. Since the zoomed out graph (Figure 29 c) insert) contains no peak it was zoomed into to display the peaks that is seen in Figure 29 c) where the peak increases with increase in scan rate. From graph c (AgFe-TiO_2) to graph d (AgFe-TiO_2-rGO) the peaks can be seen to have drastically decreased indicating the effect rGO has on the composite which is the decrease oxidation and reduction peaks resulting in the decrease in transfer of electrons. The estimated ΔE_p for a) Bare GCE, c) AgFe-TiO_2 and d) AgFe-TiO_2-rGO is 0.25 V, 1.06 V and 0.268 V respectively. This facilitates the enhanced conduction pathways with the modified catalysts, with AgFe-TiO_2 having the highest electron kinetic transport. The diffusion coefficient for AgFe-TiO_2-rGO and AgFe was 2.44 x 10^{-5} $cm^2.s^{-1}$ and 2.39 x 10^{-5} $cm^2.s^{-1}$ respectively. This is roughly the same and is an indication of the similarity of the diffusion that might occur in each of these composites.

Optimization of photocatalysis system

The concentration of pollutant and solution pH may impact on their removal from contaminated water. Therefore it was necessary to investigate the effect of these two parameters on the degradation of orange II dye that was selected as the model pollutant.

6.1 Effect of initial concentration of Dye (Orange II)

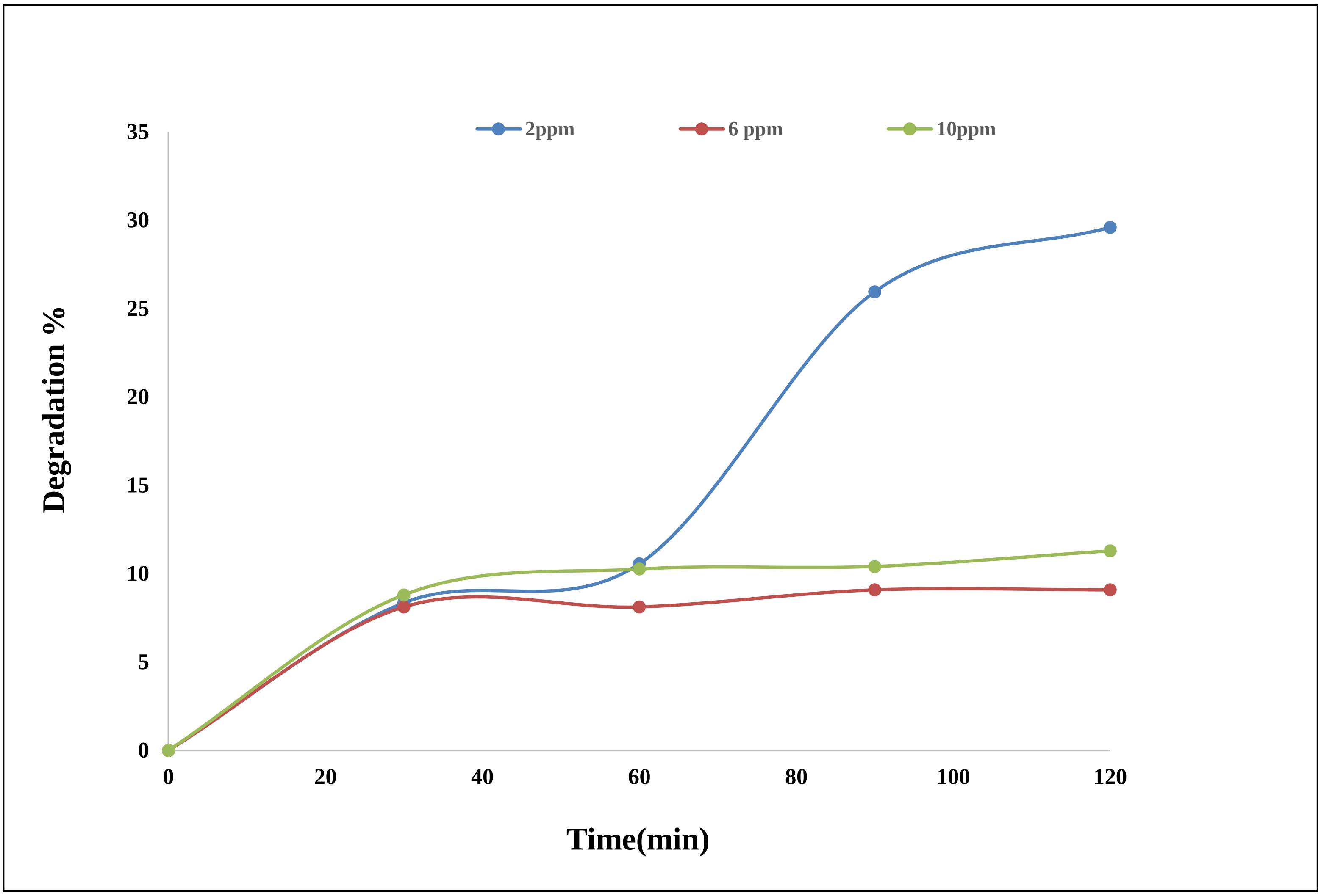

Figure 30: Graph illustrating the effect of concentration on the dye (Orange II) degradation percentage at the following conditions. Varied parameters: Dye concentration from 2, 6 to 10 ppm. Fixed parameters: pH, solution volume 500 ml, irradiation time120 min, distance between lamp and solution 5cm.

Figure 30 presents the effect of initial concentration of dye on the degradation percentage at the applied conditions. Though literature sustains that the initial concentration of the pollutant has an impact on its removal from polluted water. That is, the degradation percentage of the pollutant may decrease with increase of its initial concentration (Reza, Kurny, & Gulshan, 2017). So from the results plotted in figure 30 the trend between initial concentration and percentage degradation claimed in the literature was not observed. Nevertheless, higher removal of orange (II) was achieved at lower concentration 2 ppm. For example at minute 90 concentration 10, 6 and 2ppm had 10, 8 and 27% degradation respectively. Even though 2 ppm appeared as the best concentration in this case a reasonable concentration of dye needed to be defined to meet the sensitivity conditions of the extended analytical method such as HPLC analysis, therefore 4ppm was chosen as the working concentration of orange (II) used throughout all experiments conducted in this photocatalysis study.

Apart from dye concentration the effect of solution pH on orange (II) degradation percentage was also investigated.

6.2 Effect of solution pH on Dye (Orange II)

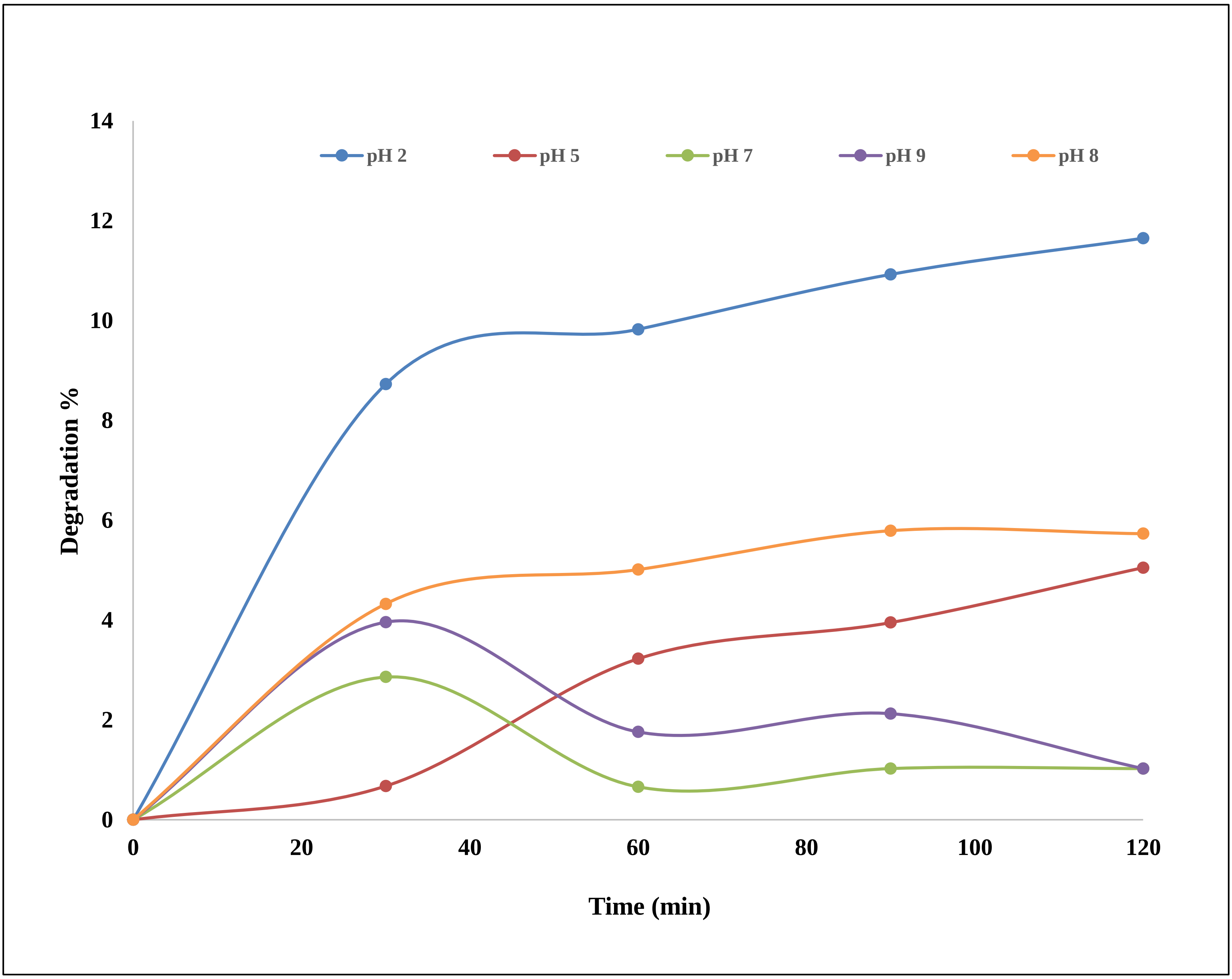

Figure 31: Graph illustrating the effect of solution pH on orange II degradation percentage at the following condition. Varied parameters: Solution pH from 2, 5 to 9. Fixed parameters: Dye concentration 4ppm, solution volume 500ml, irradiation time 120 min and distance between lamp 5cm.

Figure 31 presents the effect of solution pH on dye percentage removal at the applied conditions. According to literature pH may effect percentage degradation (Reza et al., 2017). That is, the degradation percentage of pollutant may increase with a decrease in solution pH. In Figure 31 there is however no consistent observable trend, nevertheless at the highest pH values the lowest percentage degradation was observed and at the lowest, pH 2, experienced the greatest percentage degradation. Second to pH 2 was pH 8 and this is because the base used (NaOH) to establish the pH had an influence on the percentage degradation (likewise with pH 9) as well as the temperature. It was also observed that pH 5 presents a percentage degradation below that of pH 8 and that correlates with the trend stated in literature. An example of this can be seen at minute 60 where pH 2, 5, 7, 8 and 9 had degradation percentages of 9.83, 3.23, 0.66, 5.01 and 1.76 respectively. Thus pH 2 appeared as the best pH for percentage degradation for the pollutant Orange (II). Therefore pH 2 was used as a working pH of Orange (II) and throughout all experiment conducted in this photocatalyst study.

After the photocatalysis system was optimized the following parameters dye concentration 4ppm, solution pH 2 were chosen as optimum factors that were associated to fixed parameters. Including solution volume 500 ml, irradiation time 2 hours, distance between lamp and solution 5 cm. Therefore the aforementioned optimum conditions were used to assess the photocatalytic activity of the catalysts (TiO_2 Degussa, TiO_2 Nano spheres, TiO_2 nanotubes) and the effect of catalyst dosage on the degradation percentage of dye, respectively.

6.3 Photocatalytic degradation effect of the catalysts on Dye (Orange II)

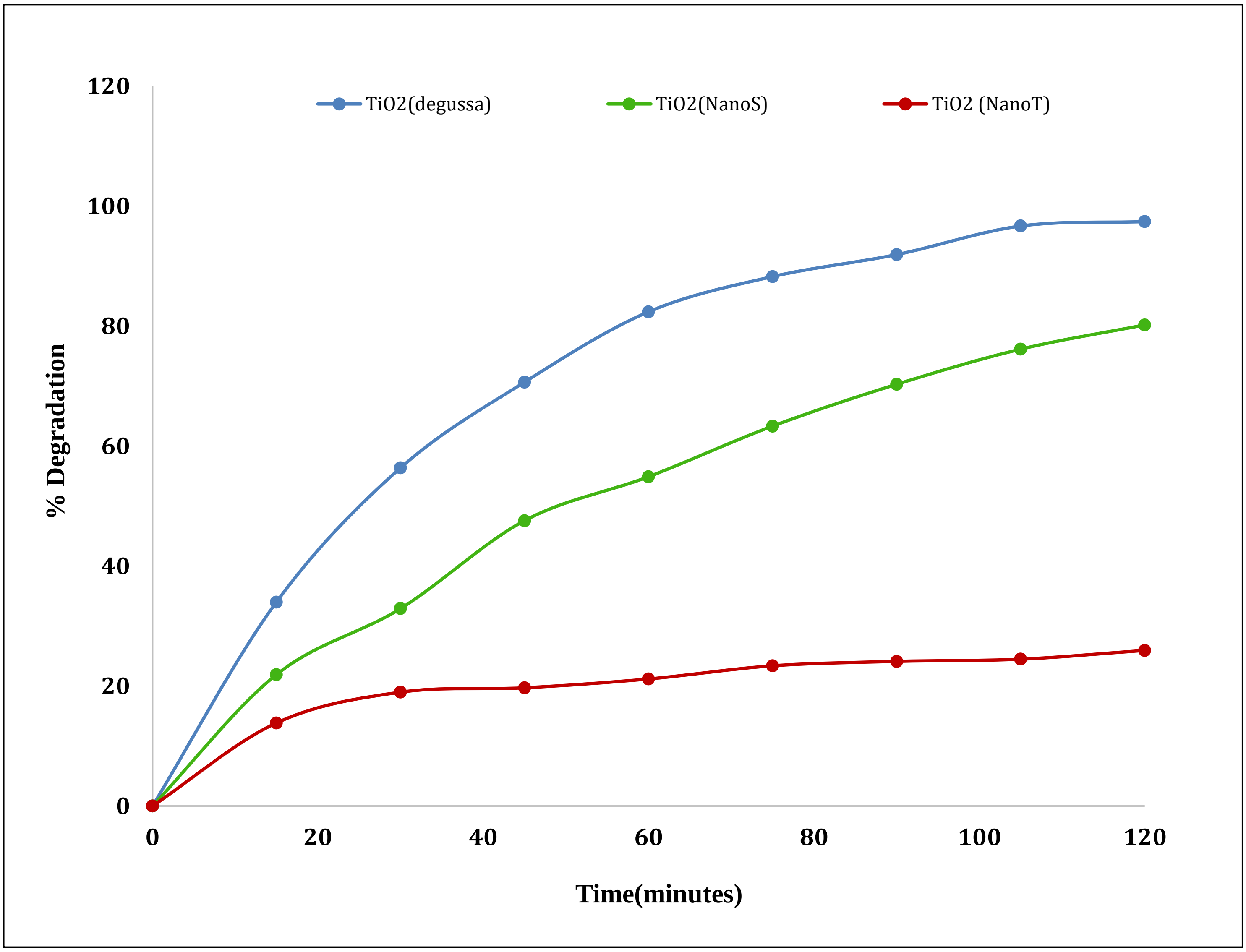

Figure 32: Graph illustrating the photocatalytic activity of TiO_2 (TiO_2 Degussa, TiO_2 nanospheres, TiO_2 nanotubes based catalysts on dye degradation percentage at the following experimental conditions. Solution pH 2, concentration 4ppm, mass of catalyst 0.01g, solution volume 500ml, irradiation time 2hours, distance between lamp and solution 5cm.

Figure 32 presents the photocatalytic activity of the catalysts (TiO_2 Degussa, TiO_2 nanospheres, and TiO2 nanotubes) under the established optimum conditions. It is observed that TiO_2 degussa had the highest percentage degradation and TiO_2 had the lowest percentage degradation. An example of this can be seen at minute 60 TiO_2 Degussa, TiO_2 nanospheres and

TiO_2 nanotubes had degradation of 82.41%, 54.91% and 21.19% respectively. This is due to the size of the nanoparticles and in turn its dispersion in the Orange (II) solution. Therefore TiO_2 was selected as the best catalyst for this photocatalytic study.

Since TiO_2 degussa was the best catalyst for the degradation of Orange (II) in this study, the impact of its amount on degradation percentage of dye was also investigated.

6.4 Effect of photocatalyst dosage on dye (orange II) degradation efficiency

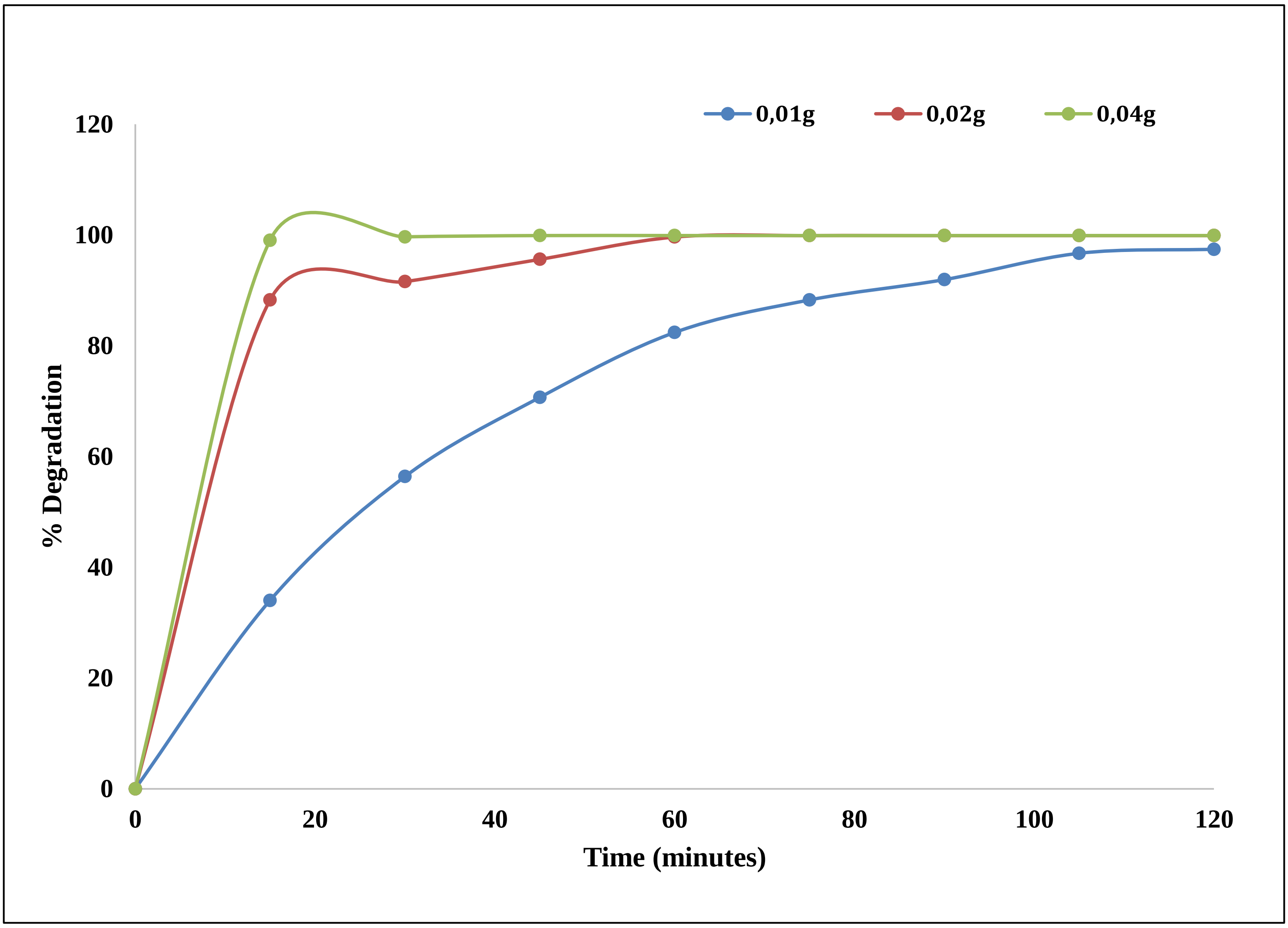

Figure 33: Illustration of the effect of TiO_2 (Degussa) dosage on percentage degradation of dye. Experimental conditions. Varied parameters: Mass of TiO_2 (Degussa) 0.01g, 0.02g and 0.04g. Fixed parameters: solution pH 2, concentration 4ppm, solution volume 500ml, irradiation time 2hours, distance between lamp and solution 5cm.

Figure 33 presents the effect of photocatalyst dosage on Orange (II) percentage degradation. Literature sustains that the mass of the catalyst has an impact on its removal (Reza et al., 2017). That is the degradation percentage of the pollutant increases with increase in mass/dosage of TiO_2 (Reza et al., 2017). So from the results plotted in Figure 33 the trend between mass of catalyst and percentage degradation was observed to confirm that. An example of this trend is observed at minute 30 where 0.01g, 0.02g and 0.04g of TiO_2 observed degradations of 56.38%, 91.57% and 99.67% respectively. Therefore it was observed that the higher the dosage of TiO_2 the greater the percentage degradation.

6.5 Effect of different photocatalyst on Orange II dye degradation

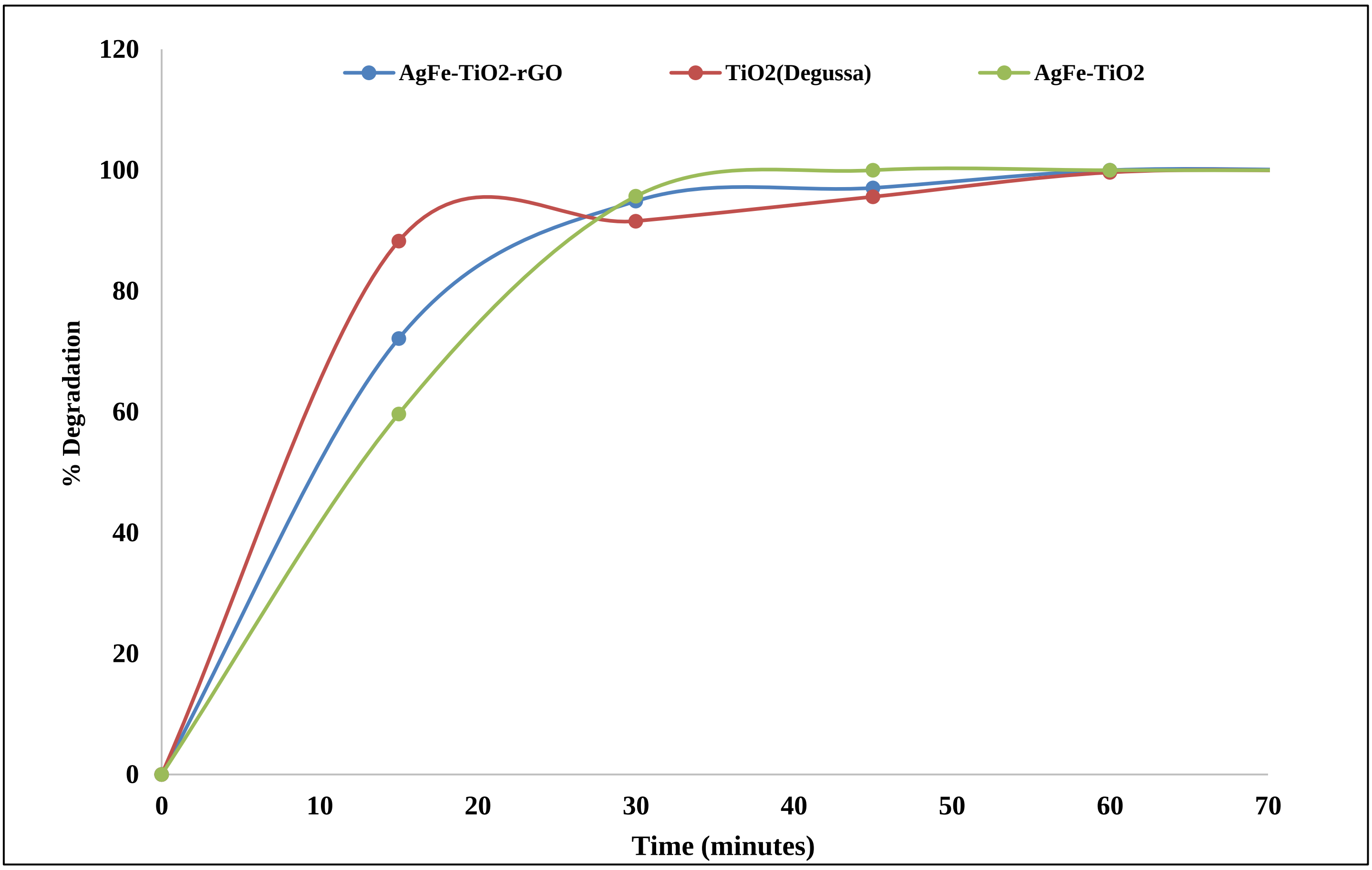

Figure 34: Illustration of the effect of the different photocatalysts TiO_2 (Degussa), AgFe-TiO_2 and AgFe-TiO_2-rGO on percentage degradation of dye. Experimental conditions. Fixed parameters: solution pH 2, concentration 4ppm, solution volume 500ml, irradiation time 2hours, distance between lamp and solution 5cm and 0.04g of each photocatalyst.

Figure 34 presents the effect of the different photocatalysts on Orange (II) percentage degradation. The degradation percentage of the pollutant should increase with all three photocatalysts. So from the results plotted in Figure 34 the trend between the type of photocatalyst and percentage degradation, the following was observed. From 0 – 30 minutes the TiO_2 degussa degraded the dye at a faster rate than both AgFe-TiO_2 and AgFe-TiO_2-rGO with AgFe-TiO_2 reacting the slowest with the dye. This is due to the surface area of the TiO_2 degussa that is greater than that of the AgFe-TiO_2 and AgFe-TiO_2-rGO However the faster degradation of the dye via the photocatalyst AgFe-TiO_2-rGO compared to the AgFe-TiO_2 photocatalyst is due to the pockets that was formed in the nanocomposite of AgFe-TiO_2-rGO (observed in Figure 24 b) which would allow for the Orange II dye molecules/particles to be stored inside instead of being photocatalysed which allows for the misguided observation that it seems to be the better photocatalyst of the two when in actual fact that result does not correlate with that of the findings of UV which through calculation indicated that the band gap of AgFe-TiO_2 and AgFe-TiO_2-rGO were 2.77 eV and 3.02 eV respectively implying that the better photocatalyst is AgFe-TiO_2. That however is confirmed from 30 -70 minutes where it is observed that the best photocatalyst is AgFe-TiO_2, and the weakest is the TiO_2 degussa, which has a UV band gap of 2.93 eV, and compared to AgFe-TiO_2-rGO (UV band gap of 3.02 eV) should be weaker, but as mentioned this could be caused by the rGO pockets created in the AgFe-TiO_2-rGO nanocomposite. Therefore it was observed that the AgFe-TiO_2 photocatalyst displayed the best overall photocatalytic activity.

Chapter 7

7.1 Conclusion

The aim of this project was to investigate Titanium dioxide modified by creating a two composites using the nanobimetal/nanoalloy silver-iron (AgFe) and reduced graphene oxide (rGO) as an improved photocatalyst for removal of contaminants such as dye from water. Different Titanium Dioxide (TiO_2) was synthesised using a hydrothermal method and TiO_2 degussa (the purchased TiO_2 nanopowder) was used as the best form of the catalyst, since it illustrated faster photocatalysis during the photocatalytic study. The TiO_2 degussa contained nanoparticles of size 15 nm – 25 nm. These dimensions would prove to enhance the dispersion of the photocatalyst in the water and therefore increase its possible collision, and in turn increase its reactivity. However its interaction affinity and reactivity efficiency can be further enhanced through the addition of the nanomaterials silver-iron alloy and possibly reduced graphene oxide. The nanocomposites AgFe-TiO_2 and AgFe-TiO_2-rGO were successfully synthesised and was evident in the morphological studies. The anatase phase of the TiO_2 degussa and nanocomposites AgFe-TiO_2 and AgFe-TiO_2-rGO were confirmed through XRD and FTIR therefore serving as a support for the maintained phase of the TiO_2 even after modification. The d-spacing for AgFe-TiO_2 and AgFe-TiO_2-rGO was calculated to be 2.22 nm and 3.25 nm, which favoured AgFe-TiO_2 in terms of photocatalysis. The XRD results along with HRTEM further indicate that both are crystalline in nature where AgFe-TiO_2 shows a higher degree of crystallinity due to the rGO in AgFe-TiO_2-rGO which is amorphous. The diffusion coefficients for TiO_2, AgFe-TiO_2-rGO and AgFe-TiO_2 were 9.07×10^{-7} $cm^2.s^{-1}$, 2.44×10^{-5} $cm^2.s^{-1}$ and 2.39×10^{-5} $cm^2.s^{-1}$ respectively. FTIR confirmed the presence of the AgFe nanoalloy in both AgFe-TiO_2 and AgFe-TiO_2-rGO as well as the rGO in AgFe-TiO_2-rGO. FTIR along with HRSEM-EDS confirmed that the precursor TiO_2 degussa and nanocomposites AgFe-TiO_2 and AgFe-TiO_2-rGO contained both Silver, Iron, Titanium and oxygen along with carbon (for graphene), where there was a silver favoured silver:Iron percentage ratio (0.85 % : 2.62 %) in AgFe-TiO_2 than in AgFe-TiO_2-rGO (5.72% : 7.24%) which was also confirmed in FTIR where at the band range of 1250 cm^{-1} - 1765 cm^{-1} (red box) contained shorter bands and the first band in the double banded filled red box (1250 cm^{-1} - 1765 cm^{-1} band range) was longer (since there was a higher silver percentage in the silver : iron ratio) than the left which was the opposite in the spectrum of AgFe-TiO_2-rGO where the second band in the double banded filled red box (1250 cm^{-1} - 1765 cm^{-1} band range) was longer/shaper than the other and this indicated an iron favoured silver : iron percentage ratio. This has proved to be significant during the photocatalytic study. HRSEM has also confirmed the morphology of AgFe-TiO_2 and AgFe-TiO_2-rGO where it was evident that AgFe-TiO_2 had a more agglomerated spherical morphology compared to AgFe-TiO_2-rGO where there were sheet-like rGO structures that created pockets that could cause potential "mistaken- photocatalysis" (where the photocatalyst appeared to be reacting more effectively with the catalyst when in actual fact the dye particles weren't being converted into free radicals but in this case hidden/stored in the rGO formed pockets giving the idea/misinterpretation of photocatalysis). This was confirmed in the photocatalytic study where the AgFe-TiO_2-rGO behaved "better" than AgFe-TiO_2 initially (first 30 minutes in Figure 33) but was however the opposite for the rest of the time (1h 30 minutes). This was further confirmed with UV where the band gap for AgFe-TiO_2-rGO was 3.02 eV compared to AgFe-TiO_2 which had a band gap of 2.77 eV therefore indicating that AgFe-TiO_2 would be the better photocatalyst. This was confirmed in the photocatalytic study where AgFe-TiO_2 was proven as the best catalyst to convert the dye (Orange II) into free radicals and ultimately remove the contaminant from the water compared to AgFe-TiO_2-rGO.

7.2 Future work

GC/MS spectroscopy is needed to identify the intermediates and final products of the dye (Orange II) degradation as well as a hydroxyl radical formation study to ensure the efficiency of the photocatalyst. HRTEM which was used cannot determine the bimetallic nature of the AgFe bimetal. In future work Brunauer –Emmett-Teller (BET) analysis will be carried out to determine the specific surface area of the materials. Those results may be used to further prove the above mechanism for enhanced photocatalysis. The Dye (Orange II) was used as an organic contaminant in this study however further study into inorganic contaminants such as nitrates, which present health concerns in rural areas with groundwater being the main source of water, may be employed to further test the efficiency of the proposed photocatalyst.

REFERENCES

1) Von Bormann, T. and Gulati, M. The Food Energy Water Nexus:WWF-SA, (**2014**)

2) Zyoud, Ahed, et al. "Optimizing photo-mineralization of aqueous methyl orange by nano-ZnO catalyst under simulated natural conditions." *Journal of Environmental Health Science and Engineering* 13.1 (**2015**): 46.

3) Methyl orange, Material safety data sheet, statement of hazardous nature. sc-206030: (**2011)**

4) Eljiedi, Arwa Alseddig Ahmed, and Azlan Kamari. "Removal of methyl orange and methylene blue dyes from aqueous solution using lala clam (Orbicularia orbiculata) shell." *AIP Conference Proceedings*. Vol. 1847. No. 1. AIP Publishing, (**2017).**

5) Awuah E., Nyarko K.B., Owusu P.A., & Osei-Bonsu K. Desalination, 248, (**2009**): 453-459.

6) Chong MN, Jin B, Chow CW, Saint C. Water Res. 44, (**2010):** 2997–3027.

7) Gaya UI, Abdullah AH. J Photochem Photobiol A Chem. 9: (**2008)** 1–12

8) Zhu K., Neale N. R., Miedaner A. and Frank A. J., Nano Lett. 7: (**2007)**, 69–74

9) Beranek R., Tsuchiya H., Sugishima T., Macak J. M., Taveira L., Fujimoto S., Kisch H. and Schmuki P.,Appl.Phys. Lett. 87: (**2005)**, 243114

10) Roy P., Berger S. and Schmuki P., Angew. Chem. Int. Ed. 50: (**2005)**, 2904–2939

11) Lazar MA, Varghese S, Nair SS. Catalysts. 2: (**2004)**, 572–601.

12) Takeuchi M., Yamashita H., Matsuoka M., Anpo M., Hirao T., Itoh N., and Iwamoto N., Catal. Lett. **67**: (**2000)** 135.

13) Linsebigler A. L., Lu G., and Yates J. T. Jr., Chemical Reviews, 95, 3: (**1995)**, 735–758

14) Pável C. Hernández D. C, Saúl R. M., Facundo R., Soft Nanoscience Letters. 4: (**2014)**, 53-62.

15) Li W, Shah, S. I. Huang, C. P, Jung, O, Ni, C. Mater. Sci. Eng. *B 96*, 247. (**2002)**.

16) Fernndez-Garca, M, Martnez-Arias, A, Hanson, J. C, Rodriguez, J. A. Chem. Rev. 104: (**2014)**, 4063.

17) Ai B, Duan X, Sun H, Qiu X, Wang S. Catal. Today, in press, (**2015).**

18) Liu J, Huang J.H, Zhou H, Antonietti M. ACS Appl. Mater. Interfaces. 6: (**2015)**, 8434–8440

19) Wang X., Maeda K., Chen X., Takanabe K., Domen K., Hou Y., Fu X., Antonietti M., Journal of the American Chemical Society. 131: (**2010)**, 1680.

20) Yan H., Yang H., Journal of Alloys and Compounds. 509, L26, (**2011).**

21) Adekoya O. D, Muhammad T, Nor A. S. A., Malaysian Journal of Fundamental and Applied Sciences. 11,3, (**2015**) : 102-105**.**

22) Zheng, Z. K, Huang, B. B, Qin, X. Y, Zhang, X. Y, Dai, Y, Whangbo, M. H., J. Mater. Chem. 21: (**2011)**: 9079−9087.

23) Liang, W. J, Li, J, Jin, Y. Q. Build. Environ. 51: (**2012)**, 345−350.

24) Sondra Ayadi, Cristian Perca,and Ludovic Legrand, Nanoscale Res Lett. 8(1): (**2013)**, 95

25) Yanfeng Chen, Weixin Huang, Donglin He, Yue Situ, and Hong Huang, ACS Appl. Mater. Interface: (**2014)**, 14405–14414

26) Umebayashi T, Yamaki T, Itoh H. and Asai K., J. Phys. Chem. Solids. 63 : (**2002)**, 1909–1920.

27) Y. K. Lai, H. F. Zhuang, K. P. Xie, D. G. Gong, Y. X. Tang, L. Sun, C. J. Lin and Z. Chen, New J. Chem.34: (**2010)**, 1335–1340.

28) Zhu J, Zheng W, He B, Zhang J. and Anpo M., J. Hazard. Mater. 216: (**2004)**, 35–43

29) Zhou, M, Yu, J, Cheng, B., J. Hazard. Mater. 137: (**2006)**, 1838–1847.

30) Mishra T. , Mahato M. ,Noor Aman, J. Patel, N, Sahu. R. K. Catal. Sci. Technol. 1: **(2011)**, 609-615.

31) Markowska-Szczupak A, Ulfig K, & Morawski A. W. Catalysis Today. 169, 1: (**2011)**, 249-257.

32) Ohno T, Sarukawa K, Tokieda K, and Matsumura M. Journal of Catalysis. 203: (**2001)**, 82-86.

33) Cong Y, Zhang J, Chen F. Journal of Physical Chemistry C. 111: (**2007)**, 10618–10623

34) Serpone N, Journal of Physical Chemistry B. 110: (**2006)**, 24287– 24293.

35) Ping Lei, Feng Wang, Xiaowei Gao, Yanfen Ding, Shimin Zhang, Jincai Zhao, Shaoren Liu, Mingshu Yang., Journal of Hazardous Materials: (**2013)**, 227–228, 185–194,

36) Khan, Mohammad Mansoob, Syed Farooq Adil, and Abdullah Al-Mayouf. "Metal oxides as photocatalysts." **(2015)**: 462-464.

37) Ping. C, Zhi. Y , Hong. W, Wei. C , Mingxia. C, Wenfeng .S, Guifu D. international journal of hydrogen energy .37: (**2012)**, 2224 -2230

38) Akwensioge, Mbinze. The influence of anthropogenic nitrate on groundwater quality in the Thaba Nchu area. Diss. University of the Free State, **(2012)**.

39) Reiner, Monika. "Industrial waste minimisation in South Africa: A case study in the textile and metal finishing sectors by." (**2002**).

40) Helmer, Richard, Ivanildo Hespanhol, and World Health Organization. "Water pollution control: a guide to the use of water quality management principles." (1**997**).

41) Woodford, Chris, Calhoun, Yael, Seideman, David, Environmental chemistry module 1. "Water Pollution." (**2015**)

42) Enderlein, Rainer, Williams. "Water quality control". (**1997**)

43) Su, Claire Xin-Hui, et al. "Combination and hybridisation of treatments in dye wastewater treatment: a review." *Journal of Environmental Chemical Engineering* 4.3 (**2016**): 3618-3631.

44) Yadav, V. S. K., and M. K. Purkait. "Concurrent electrochemical CO 2 reduction to HCOOH and methylene blue removal on metal electrodes." *RSC Advances* 6.47 (**2016**): 40916-40922.

45) Li, Fu, et al. "Enhanced removal of azo dye using modified PAN nanofibrous membrane Fe complexes with adsorption/visible-driven photocatalysis bifunctional roles." *Applied Surface Science* 404 (**2017**): 206-215.

46) Gadekar, Mahesh R., and M. Mansoor Ahammed. "Coagulation/flocculation process for dye removal using water treatment residuals: modelling through artificial neural networks." *Desalination and Water Treatment* 57.55 (**2016**): 26392-26400.

47) Félicien, Mazille. "Coagulation-Flocculation". (**2003**)

48) Granche, Berhe. ” Removal of colour and turbidity (coagulation, flocculation filtration)”. (**2015**)

49) Ajmal, Anila, et al. "Principles and mechanisms of photocatalytic dye degradation on TiO 2 based photocatalysts: a comparative overview." *Rsc Advances* 4.70 (**2014**): 37003-37026.

50) Shi, Jianwen, et al. "Photocatalytic degradation of methyl orange in water by samarium-doped TiO2." *Environmental Engineering Science* 25.4 (**2008**): 489-496.

51) Wold, Aaron. "Photocatalytic properties of titanium dioxide (TiO2)." *Chemistry of Materials* 5.3 (**1993**): 280-283.

52) Elsalamony, R. A. "Research & Reviews: Journal of Material Sciences."**(2016)**

53) Kobwittaya, K., and S. Sirivithayapakorn. "Photocatalytic Reduction of Nitrate over Fe-modified TiO2." *APCBEE Procedia* 10 (**2014**): 321-325.

54) Kobwittaya, Krisana, and Sanya Sirivithayapakorn. "Photocatalytic reduction of nitrate over TiO 2 and Ag-modified TiO 2." *Journal of Saudi chemical society* 18.4 (**2014**): 291-298.

55) Bharti, Bandna, et al. "Formation of oxygen vacancies and Ti3+ state in TiO2 thin film and enhanced optical properties by air plasma treatment." *Scientific reports* 6 (**2016**)

56) Ansari, Sajid Ali, et al. "Silver nanoparticles and defect-induced visible light photocatalytic and photoelectrochemical performance of Ag@ m-TiO 2 nanocomposite." *Solar Energy Materials and Solar Cells* 141 (**2015**): 162-170.

57) Kumari, R. Mankamna, et al. "Antibacterial and photocatalytic degradation efficacy of silver nanoparticles biosynthesized using Cordia dichotoma leaf extract." *Advances in Natural Sciences: Nanoscience and Nanotechnology* 7.4 (**2016**): 045009.

58) Jang, Jum Suk, et al. "Development of a potential Fe2O3-based photocatalyst thin film for water oxidation by scanning electrochemical microscopy: effects of Ag− Fe2O3 nanocomposite and Sn doping." *Chemistry of Materials* 21.20 (**2009**): 4803-4810.

59) Pan, Xuan, et al. "TiO2/graphene nanocomposite for photocatalytic application." *Materials and Processes for Energy: Communicating Current Research and Technological Developments; Méndez-Vilas, A., Ed* (**2013**): 913-920.

60) Alam, Tanvir E. "Metal Oxide Graphene Nanocomposites for Organic and Heavy Metal Remediation." (**2012**).

61) Nanakoudis. M, What is SEM? SEM technology explained, PhenomWorld, 01 Jun (**2017)**

62) Maleki. S, TEM, Idolunion, 01 Apr (**2010**)

63) Khalil, Munawar, et al. "Electrodeposition of Iridium Oxide Nanoparticles for pH Sensing Electrodes." Journal of The Electrochemical Society 163.9 (**2016**): B485-B490.

64) Winterburn. E, “Braggs”, Wordpress, 06 Feb **(2013)**

65) Riding. T, “Graphene”, Lorentin, 4 Jan (**2011)**

66) Schwarz, James A., Cristian I. Contescu, and Karol Putyera, eds. Dekker encyclopedia of nanoscience and nanotechnology. Vol. 3. CRC press, **(2004)**

67) Bakan, Feray, et al. "Structural and Chemical Analysis of Hydroxyapatite (HA)-Boron Nitride (BN) Nanocomposites Sintered Under Different Atmospheric Conditions." Microscopy and Microanalysis 23.5 (**2017**): 891-899.

68) Fresno, F., et al. "Influence of surface density on the CO 2 photoreduction activity of a DC magnetron sputtered TiO 2 catalyst." Applied Catalysis B: Environmental 224 (**2018**): 912-918.

69) Pal, Jolly, et al. "Removal of methyl orange by activated carbon modified by silver nanoparticles." Applied Water Science 3.2 (**2013**): 367-374.

70) Kumar, A., and G. Pandey. "A Review on the Factors Affecting the Photocatalytic Degradation of Hazardous Materials." Material Sci & Eng Int J 1.3 (**2017**): 00018.

71) Theivasanthi, Thirugnanasambandan, and Marimuthu Alagar. "Titanium dioxide (TiO2) Nanoparticles XRD Analyses: An Insight." arXiv preprint arXiv (**2013**):1307.1091